Femtosecond Carrier Dynamics in AlGaAs

by

Morrison Ulman

B.S.E., Princeton University
(1988)

Submitted to the Department of Physics in partial fulfillment
of the requirements for the degree of

Doctor of Philosophy

at the

Massachusetts Institute of Technology

June, 1994.

© Massachusetts Institute of Technology 1994.

Signature of Author_____
Department of Physics
June 10, 1994

Certified by_____
Prof. James G. Fujimoto
Thesis Supervisor

Accepted by_____
Prof. George F. Koster
Chairman of the Graduate Committee

1

Femtosecond Carrier Dynamics in AlGaAs
by
Morrison Ulman

Submitted to the Department of Physics on June 10, 1994 in partial fulfillment of the requirements for the degree of Doctor of Philosophy.

Abstract

The femtosecond dynamics of electrons and holes in AlGaAs are sutdied by combining femtosecond laser spectroscopy and ensemble Monte Carlo simulation.

A femtosecond pulsed laser system is used to investigate ultrafast dynamics in the semiconductor via pump-probe spectroscopy. An ultrashort optical pulse focussed on the sample excites a transient carrier distribution. The evolution of this distribution is determined from transmission measurements of a probe pulse which is delayed for some time after the exciting ("pump") pulse. The delay between the pump and probe pulses is varied in sub-femtosecond steps so the measurement time resolution is limited only by the laser pulse duration which is 40 femtoseconds.

The nonlinear optical response of the material is caused by the dynamics of electrons and holes. They are characterized by an energy distribution function. In thermal equilibrium the distribution function is the Fermi function multiplied by the density of states. After optical excitation, however, the distribution is non-thermal. In fact its shape reflects the spectrum of the exciting optical pulse and the allowed optical transitions in the system. The non-equilibrium distribution thermalizes in approximately 100 fs and cools to the lattice temperature in about 1000 fs.

Pump-probe data are measurements of pump pulse induced changes in the transmission of the probe pulse through the sample. These data do not directly reveal the underlying carrier distributions, however. Accurate modelling is complicated by the need to take into account several optical transitions and many carier relaxation mechanisms. In collaboration with theorists at the University of Florida we are able to establish correspondence between our experimental results and predicted carrier distributions through the use of ensemble Monte Carlo simulations.

The theory fits the data well and and may be used to predict behavior in future experiments and possibly AlGaAs optoelectronic devices.

Thesis supervisor: James G. Fujimoto
Title: Professor of Electrical Engineering

Acknowledgements

It is a great pleasure to mention just a few of the many people who have helped me during my time at MIT.

No one is more deserving of my thanks than my adviser, Jim Fujimoto. From careful observation of him and endless pondering over his cryptic comments I absorbed a tiny bit of his wisdom. It took me several years to appreciate his Buddha-like management style. He has provided an enriching intellectual environment and convinced the US government to spend hundreds of thousands of dollars to support it.

I thank Professors Robert J. Birgeneau and Wolfgang Ketterle for serving on my thesis committee and for their comments on this thesis.

I was lucky to work directly with many top notch experimentalists in the lab including Lucio Acioli, Bob Schoenlein, Malini Ramaswamy, Guiseppe (I am) Gabetta, and Igor Bilinsky.

Theoretical support for this work (and for other projects in our group) comes from the outstanding efforts of Professors Dan Bailey (University of South Carolina) and Chris Stanton (University of Florida).

Mike LaGasse and Katie Hall, my original office mates, introduced me to the dark side of graduate school.

Kazu Naganuma, solver of the crazy dinosaur problem, arranged a fascinating trip to Japan and NTT. It was a highlight of my graduate career.

I gained valuable physical insight from the creative minds of Jyhpyng Wang and Stuart Brorson.

Special thanks to Charlie Hultgren for stimulating gaseous (sometimes flammable) emissions, popularizing the word "wookie" and a whole vocabulary to go with it, introducing me to burritos, being a fellow III-V man, and being a trusted adviser on a veritable armada of issues. His legend will live in the halls of building 36 for at least a week after he graduates. World traveller Joe Jacobson was a cohort in adventures near MIT and around the globe. His extensive discourse (about 50% based on hard facts) spanned everything from quantum electrodynamics to proper interpretation of Fujimotoisms. I look forward to rejoining his juggernaut in California.

DH, DD, KB, JG, GL, JI, MM, MB, and MB are valued friends; I hope I will see much more of them in the future.

Thanks to roommates SA, SB, BG, RL, CB, JH, JH, and HJ for making life in Somerville and Cambridge enjoyable, and, in the case of the last three, for demonstrating the fine art of slugdom.

Thanks to my family for their love, enthusiasm for MIT, and blissful ignorance of what really happens there.

Contents

Chapter 1
Introduction

1.0 Objectives

This thesis describes a series of experiments that were performed with the goal of improving our understanding of ultrafast carrier dynamics in AlGaAs. We want to know how hot carriers in a semiconductor relax toward the band edge in the first picosecond after photoexcitation. Ideally we would like to be able to predict the time evolution of the carrier distribution function in a semiconductor with femtosecond resolution. This knowledge has both practical and fundamental appeal.

From a fundamental point of view, nonequilibrium dynamics is an area of active research. The statistical mechanics of electrons in equilibrium is well known; the distribution is described by the Fermi function. Out of equilibrium, changes in the distribution function are described by the Boltzmann equation which is a form of continuity or bookkeeping equation.

The practical motivation for this work is that GaAs is an important material for high speed device fabrication [1][2]. Once we have developed an accurate model for carrier behavior in bulk semiconductors we will have completed an important step on the road to realistic device modelling and device design.

Intimately related to our goal of improved understanding of the AlGaAs system is our work in developing femtosecond laser technology and Monte Carlo simulation techniques. Femtosecond laser design is an

active field and sources that directly generate optical pulses as short as 10 femtoseconds have recently been announced [3]. It remains to build widely tunable femtosecond lasers at visible wavelengths. Of course, as Gert t'Hooft remarked, if one's laser is tunable it just means that the pulses are not short enough. On the theoretical side when Monte Carlo simulation is used to solve the Boltzmann equation we assume instantaneous scattering times and classical trajectories for particles between scattering. We are approaching a time scale where the calculation of scattering rates by Fermi's Golden Rule may break down and quantum coherences become important.

1.1 Approach

We combine femtosecond laser spectroscopy with ensemble Monte Carlo simulation in a joint experimental and theoretical program. Experimentally, we use a femtosecond laser system based on an amplified, colliding-pulse-modelocked, ring dye laser. This system produces pulses as short as 3×10^{-14} seconds with megawatt peak powers. We have used nonlinear optical techniques to generate femtosecond pulses at wavelengths tunable from 620 to 720 nm. These pulses are used in pump-probe transient absorption saturation spectroscopy. The transmission of a probe pulse through a sample is recorded versus pump-probe delay. The time resolution of the pump-probe technique is limited only by the duration of the optical pulses.

We have formed a collaboration with theorists at the University of Florida to help interpret our experimental results and construct an accurate computer model for the electron dynamics. Our theoretical analysis proceeds in three steps. First the relevant semiconductor

bandstructure is calculated and scattering rates and optical matrix elements are determined. Second the electron and hole dynamics are tracked in an ensemble Monte Carlo simulation. The simulation records the carrier distribution as they evolve in time. Finally, the calculated distributions are used to predict the experimentally measured transient absorption saturation data.

1.2 Significance

Femtosecond lasers provide the highest time resolution spectroscopic measurement technique available today. They permit us to investigate the fundamental scattering processes in a semiconductor on the same time scale that those processes occur.

Ensemble Monte Carlo simulation is the only method that allows us to examine the effect of several different possible scattering mechanisms in a real semiconductor. It is neccessary to take into account the many possible optical transitions and scattering channels in order to develop an accurate model of carrier dynamics. Because the Monte Carlo simulation technique is unique in its ability to handle the complexities of the AlGaAs system, it is a neccessity in our work.

GaAs is important for many high speed electronic devices such as tunnel diodes and transferred electron devices [1][2]. It is used in photonic applications such as semiconductor lasers, photodiodes and optical modulators. In order for photonics to replace today's electronics, photonic devices will have to operate in the picosecond or faster regime. Electronic devices already operate at 10 GHz and some are approaching 100 GHz so optoelectronics must be faster to be useful. The speed of

GaAs electronics and optoelectronics is ultimately limited by the fundamental carrier dynamics.

1.3 Structure of the thesis

Chapter 2 provides a brief history of results in the field and points out some landmark experimental and theoretical developments. Chapter 3 describes the laser systems and nonlinear optical techniques used to perform the experiments. Chapter 4 discusses the theory of carrier scattering in semiconductors and Monte Carlo modelling of carrier dynamics. Chapter 5 presents the results of a tunable femtosecond study of hot carriers in $Al_{0.1}Ga_{0.9}As$. Chapter 6 describes femtosecond experiments on GaAs and $Al_{0.2}Ga_{0.8}As$ samples in which we investigated the effect of a background plasma of cold carriers on the relaxation of hot carriers. Chapter 7 is the conclusion and contains sugestions for future work.

Appendix A describes some recent work on femtosecond scanning tunnelling microscopy.

1.4 References

[1]   B. G. Bosch and R. W. H. Engelmann, Gunn-effect Electronics, John Wiley & Sons, New York, 1973.

[2]   S. M. Sze, Semiconductor Devices: Physics and Technology, John Wiley & Sons, New York, 1985.

[3]   M. T. Asaki, C. P. Huang, D. Garvey, J. Zhou, H. C. Kapteyn, and M. M. Murnane, "Generation of 11 fs pulses from a self modelocked Ti:sapphire laser," Optics Letters 18, p. 977 (1993).

Chapter 2
Review of femtosecond carrier dynamics in semiconductors

2.0 Introduction

In this chapter we point out some of the important work that has been published on hot carrier dynamics in semiconductors. The subject is broad so we concentrate specifically on experimental results obtained with picosecond and femtosecond lasers and theoretical work using Monte Carlo simulations.

Hot carrier dynamics in semiconductors has been investigated in a wide variety of ways [1]. Techniques that have been applied to study carrier dynamics include velocity vs. field measurements, hot-electron charge transport measurements [2], absorption, and luminescence. The invention of ultrafast modelocked lasers has revolutionized the field because it has enabled researchers to study carrier scattering on the same time scale that the scattering occurs.

On the theoretical side, before the advent of high speed computers most investigations concentrated on analytical calculations of scattering rates. In the last ten years much more emphasis has been placed on computer simulations of complicated systems [3]. Just recently detailed correspondence between theory and experiment has begun to be achieved.

2.1 Experimental studies

Soon after the development of the picosecond dye laser [4] picosecond pump-probe spectroscopy was applied to investigate the dynamics of carriers in semiconductors. In an early pump-probe [5] experiment, Auston et al. measured time resolved reflectivity from nonequilibrium carriers in GaAs [6]. They discovered that the differential reflectivity depended strongly on carrier temperature. Shank et al. were then able to investigate band edge absorption in GaAs with subpicosecond resolution and concluded that a hot carrier distribution cools to the lattice temperature (80 K in that experiment) with an exponential time constant of 4 ps [7]. Around the same time that Shank's experiments were performed at AT&T Bell Laboratories a German group reported a picosecond pump-probe absorption experiment on GaAs in which they observed that the carrier relaxation rate decelerated in time [8]. They determined that the carrier cooling mechanism was consistent with polar LO-phonon emission. These early experiments showed that it was possible to investigate nonequilibrium carrier dynamics with pulsed lasers and that the necessary time resolution was within striking distance.

A few years later Oudar et al. performed a study using polarized 250 fs pulses to measure the momentum orientational relaxation time in GaAs just above the band gap [9]. In this experiment the probe polarization was set 30 degrees away from that of the pump. The momentum distribution of excited electrons is anisotropic so the absorption of the probe is different for polarizations parallel or perpendicular to the pump. The pump induced rotation of the probe pulse was detected and a momentum relaxation time of 190 fs was estimated. The carriers in this experiment were photoexcited to energies

25 meV or less above the band edge which is too small for LO phonon emission. It was assumed, therefore, that the relaxation mechanism was carrier - carrier scattering.

Picosecond and subpicosecond luminescence spectroscopy was pioneered by Shah and applied to GaAs samples [10][11]. In Shah's experiments the luminescence signal is gated by sum frequency generation in a nonlinear crystal. One of the advantages of the luminescence method is that depending on the type of nonlinear crystal used, the detection bandwidth may extend from the visible to as far as 4 um in the infrared. Shah observed that the hot carrier cooling rate was slower than expected for phonon mediated cooling for high carrier densities. The time resolution has now been improved to approximately 60 fs.

C. L. Tang's group at Cornell began a long series of experiments using an equal pulse correlation technique in 1983 [12][13][14][15][16]. Equal pulse correlation experiments record the transmission of two equal intensity pulses through a thin sample as a function of the delay between them. The transmitted intensity is a maximum at zero delay and decays to a background level when the delay is much greater than the relaxation time of the absorption process. Tang et al. claim that the equal pulse correlation technique is useful for studying relaxation that occurs on time scales comparable to or faster than the pulse width in the presence of slower relaxation mechanisms. The equal pulse correlation signal is a narrow symmetrical peak on a flat background corresponding to the slow processes. Tang's group measured 30 to 60 fs relaxation times in GaAs and $Al_{0.3}Ga_{0.7}As$. In AlGaAs they observed a density dependent relaxation time of 30 fs for a carrier density of $6 \times 10^{19} cm^{-3}$ increasing to 60

fs for a density of $6 \times 10^{17} cm^{-3}$. In GaAs, a 35 fs relaxation was density independent. There was some controversy over these measurements, however, because the fast relaxation times measured may correspond to coherent artifacts in which pump light is scattered into the probe direction.

Tang et al. typically deconvolve double sided exponential decays from their data. They say that this is more accurate than deconvolution from pump-probe data where the slow process is often a step change in transmission at zero delay which can mask the fast process of interest. Any technique that tries to extract more than one exponential time constant from an experimental curve should be viewed with caution, however, because there is no simple way to fit a curve to a nonlinear function. In practice, multiexponential fitting is often done by eye.

At MIT, Fujimoto's group began a program of experiments in 1986 using a colliding pulse modelocked (CPM) dye laser and later an amplified femtosecond laser system [17][18][19]. These experiments investigated hot carrier scattering, energy relaxation, and intervalley scattering using pump-probe differential absorption saturation measurements.

The first series of experiments was intended to measure scattering out of hot carriers' initial photoexcited states. 35 fs pulses from the CPM were used in pump-probe measurements on $Al_xGa_{1-x}As$ for x= 0.0, 0.2, 0.3, and 0.4. The data were analyzed by subtracting a 1.5 ps long time constant response from the pump-probe traces. This left a single sided exponential which represents the decay of the initial transient response. The fast decay varied from 13 fs in GaAs to 330 fs in $Al_{0.4}Ga_{0.6}As$. This behavior is a consequence of the increasing band gap in $Al_xGa_{1-x}As$ as x

is increased. When the mole fraction, x, is increased the carriers excited by the 2 eV laser are placed at correspondingly lower energies in the conduction band. Also for the higher mole fractions investigated, the split off transitions are not possible and scattering to the X and L satellite valleys is less likely. All these factors lead to the slowing of the transient response as x is increased.

In a second series of experiments the CPM laser pulses were amplified with a copper vapor laser pumped dye amplifier. The amplified pulses were used to generate a femtosecond continuum which was used as the probe in pump-probe experiments. The CPM fundamental wavelength (620 nm, 2 eV) was used as the pump. One of the more important discoveries made during this set of experiments was that the abosorption saturation of the continuum probe has a very fast step response throughout the band, even at 1.55 eV near the band edge. At first, this was thought to be evidence that a large population of electrons scatter to the bottom of the conduction band within 200 fs. That interpretation conflicted, however, with evidence from other experiments which indicated that it takes several picoseconds for electrons to relax to the band edge. The conflict was later resolved [20] by comparison to Monte Carlo computer simulations that showed that the experimental data could only be accurately modelled if holes were included in the simulation. This was one of the first triumphs of the Monte Carlo technique applied to femtosecond carrier dynamics.

A third set of experiments used a dye laser synchronously pumped by a compressed and frequency doubled modelocked Nd:YAG laser. This system was applied to $Al_{0.3}Ga_{0.7}As$ from 580 nm to 650 nm (2.14 eV to 1.91 eV) in an investigation of intervalley scattering. It was observed that

the initial scattering time of carriers is significantly faster for photon energies which promote electrons high enough in the conduction band to scatter to the L and X satellite valleys.

W. Knox at AT&T performed a landmark series of experiments on the femtosecond dynamics of excitons in GaAs multiple quantum well structures. In one experiment the first observation of nonthermal photoexcited carrier distributions in a quantum well was reported [21]. These distributions thermalized in approximately 200 fs. It was shown that near the band edge the effect of Coulomb screening on the bleaching of 2D exciton resonances is weaker than effects due to the Pauli exclusion principle. In a second experiment, modulation doped quantum wells were studied [22]. Modulation doping means that only the walls of the quantum wells are doped. This allows one to introduce a unipolar cold carrier distribution in quantum well without suffering the effects of ionized impurity scattering. It was found that a cold population of electrons introduced by doping led to a hot carrier thermalization time too fast to be resolved (< 10 fs). On the other hand, when cold holes were introduced the thermalization time for hot carriers was close to that of undoped samples (60 fs). This was explained by the assumption that the large mass difference between electrons and holes renders electron-hole scattering essentially elastic while some inelasticity exists for electron-electron scattering.

In 1988 Shank's group reported photon echo experiments on GaAs performed with 6 fs pulses [23]. The interpretation of this experiment depends on considering the band-to-band absorption in GaAs as a set of two level transitions with Lorentzian line widths given by $4/T_2$, where T_2 is the polarization dephasing time. Shank reported that the dephasing

time varied from 14 to 44 fs as the density of carriers ranged from 7×10^{18} to $1.5 \times 10^{17} cm^{-3}$. The increase of the dephasing rate with density was interpreted as proof that the main dephasing mechanism is carrier-carrier scattering. Another candidate, screened electron-phonon scattering, decreases with density [24].

Although not discussed by Shank, the dephasing time is important in the context of Monte Carlo simulation. Dephasing is not considered explicitly in Monte Carlo simulations but is implicitly included in the initial energy bandwidth of optically excited carrier distributions. The energy spread is determined by the pulsewidth or the dephasing rate, whichever is faster.

In another experiment, Shank's group used 6 fs pulses in a study of GaAs in which the sample temperature was varied to modify the bandstructure [25]. At room temperature carrier scattering was possible to both the X and L satellite valleys, while the X valley was energetically inaccessible when the sample was cooled to 35 K. Using deconvolution techniques scattering times of 55 and 80 fs were estimated for carriers scattering from Γ to X and L respectively. After moving to Lawrence Berkeley Laboratory, Shank's group performed a similar experiment [26]. In the new version the probe transmission versus pump-probe delay was analyzed at different wavelengths in a monochromator. The new technique revealed that the scattering time from the Γ to X valley became longer in a narrow energy range near the minimum in the X valley. This was interpreted as resulting from an accumulation of carriers in the Γ valley at an energy about one intervalley phonon energy below the X valley minimum. The effect was called resonant intervalley scattering.

Peyghambarian's group performed an early study of optical nonlinearities in GaAs [27]. They measured absorption and refractive index nonliearities under quasisteady state conditions and attributed their results to band filling and plasma screening of Coulomb enhancement near the band edge.

Recently Peyghambarian's group has investigated spectral hole burning in CdSe [28] in a three pulse experiment similar to the one we describe in Chapter 6. In Peyghambarian's experiment, a "gain" pulse is incident on the back of the 2.8 μm thick sample 9 ps before a pump probe measurement is performed. They observed a spectral hole using a background carrier density of $3 \times 10^{19} cm^{-3}$ and 150 fs pump and probe pulses tuned from 690 to 715 nm. The hole appears at slightly shorter wavelengths than the pump and is spectrally wider than the pump. In time it exists near zero delay, shifts to lower energies by 40 fs probe delay, and disappears by 160 fs delay. The shifting and filling of the spectral hole is attributed to carrier - carrier scattering. Their data seem to agree with a model that treats carrier - carrier scattering by solving the Boltzmann transport equation in the relaxation time approximation.

2.2 Theory

The theory of carrier dynamics in semiconductors began with analytic calculations of bandstructure and scattering rates. Later, as high speed computers became available, Monte Carlo simulation emerged as a powerful tool for evaluating carrier scattering experiments. Here we give a brief overview of some of the developments in threoretical interpretation. The recent advances have come not from new

microscopic theories of scattering, but from the use of high speed computers to keep track of many components of a complex system.

The idea of an electric field dependent electron temperature was introduced by Frohlich in 1947 [29]. Stratton calculated the electron mobility as a function of applied field under the influence of polar optic phonon scattering [30]. Carrying on from this early work, analytical calculations concentrated on scattering rates for electrons [31][32] and holes [33][34][35]. In recent years some researchers have used empirical pseudopotential calculations to obtain intervalley deformation potentials and scattering rates [36].

Lindbergh and Koch have championed the use of semiconductor Maxwell-Bloch equations [37][38] and many body techniques to study passive and active [39] structures. Essentially they treat a two band semiconductor with a generalized Rabi frequency and compute the absorption of plane waves travelling through the system.

The most successful approach for interpreting femtosecond optical experiments on semiconductors has been the Monte Carlo simulation technique. Monte Carlo was applied to semiconductors [40] as early as 1966 and to GaAs a few years later [41]. Recently the most important Monte Carlo work has been performed by Ferry's group [42][43], by Lugli, Jacoboni, and Reggiani [44][45] in Italy, and by Stanton, Bailey, and Hess [46][47][48].

The major development in Monte Carlo simulation has been the inclusion of full bandstructure as pioneered by Hess [49]. Full bandstructure, calculated by the k•p method, leads to much more accurate Monte Carlo results than were previously possible in two band models or in parabolic band models.

2.3 Conclusion

The study of carrier dynamics in semiconductors has been an active field of research for a long time. Recently great progress has been made in time resolution and tunability of pulsed laser experiments. Theoretical advances have been highlighted by progress in the application of the Monte Carlo simulation technique. Monte Carlo is the only technique which is able to extract fundamental information at short times.

In the context of the work that has already been done it is useful to do femtosecond pump probe experiments using a tunable laser to look at intervalley scattering and the region of the conduction band between the band edge and the high excess energies of 2 eV experiments. It will also be informative to look at carrier dynamics in the presence of a cold background for fundamental as well as practical (diode laser) applications.

2.4 References

[1]   S. A. Lyon, "Spectroscopy of hot carriers in semiconductors," Journal of Luminescence **35**, p. 121 (1985).

[2]   K. Seeger in Electronic Materials, edited by N. B. Hannay and U. Colombo, Plenum, New York, 1973.

[3]   K. Hess, Advances in Electronics and Electron Physics **59**, p. 239 (1982).

[4]   E. P. Ippen and C. V. Shank, Applied Physics Letters **27**, p. 488 (1975).

[5]   E. P. Ippen and C. V. Shank, "Techniques for measurement," in Ultrashort Light Pulses edited by S. L. Shapiro, Springer-Verlag, New York, 1977.

[6]   D. H. Auston, S. McAfee, C. V. Shank, E. P. Ippen, and O. Teschke, "Picosecond spectroscopy of semiconductors," Solid State Electronics **21**, p. 147 (1978).

[7]   C. V. Shank, R. L. Fork, R. F. Leheny, and J. Shah, "Dynamics of Photoexcited GaAs Band-Edge Absorption with Subpicoseond Resolution," Physical Review Letters **42**, p. 112 (1979).

[8]   D. von der Linde and R. Lambrich, "Direct measurement of hot-electron relaxation by picosecond spectroscopy," Physical Review Letters **42**, p. 1090 (1979).

[9]   J. L. Oudar, A. Migus, D. Hulin, G. Grillon, J. Etchepare, and A. Antonetti, "Femtosecond orientational relaxation of photoexcited carriers in GaAs," Physical Review Letters **53**, p. 384 (1984).

[10]   K. Kash and J. Shah, "Carrier energy relaxation in $In_{0.53}Ga_{0.47}As$ determined from picosecond luminescence studies," Applied Physics Letters **45**, p. 401 (1984).

[11]   J. Shah, T. C. Damen, and B. Deveaud, "Subpicosecond luminescence spectroscopy using sum frequency generation," Applied Physics Letters **50**, p. 1307 (1987).

[12]   C. L. Tang and D. J. Erskine, "Femtosecond relaxation of photoexcited nonequilibrium carriers in $Al_xGa_{1-x}As$," Physical Review Letters **51**, p. 840 (1983).

[13]   D. J. Erskine, A. J. Taylor, and C. L. Tang, "Femtosecond studies of intraband relaxation in GaAs, AlGaAs, and GaAs/AlGaAs multiple quantum well structures," Applied Physics Letters **45**, p. 54 (1984).

[14]   A. J. Taylor, D. J. Erskine, and C. L. Tang, "Ultrafast relaxation dynamics of photoexcited carriers in GaAs and related compounds," Journal of the Optical Society of America B **2**, p. 663 (1985).

[15]   M. J. Rosker, F. W. Wise, and C. L. Tang, "Femtosecond optical measurement of hot-carrier relaxation in GaAs, AlGaAs, and GaAs/AlGaAs multiple quantum well structures," Applied Physics Letters **49**, p. 1726 (1986).

[16]   F. W. Wise, I. A. Walmsley, and C. L. Tang, "Experimental determination of hot-carrier scattering processes in $Al_xGa_{1-x}As$," Applied Physics Letters **51**, p. 605 (1987).

[17]   W. Z. Lin, J. G. Fujimoto, E. P. Ippen, and R. A. Logan, "Femtosecond carrier dynamics in GaAs," Applied Physics Letters **50**, p. 124 (1987).

[18]   W. Z. Lin, J. G. Fujimoto, E. P. Ippen, and R. A. Logan, "Femtosecond dynamics of highly excited carriers in $Al_xGa_{1-x}As$," Applied Physics Letters **51**, p. 161 (1987).

[19]   R. W. Schoenlein, W. Z. Lin, E. P. Ippen, and J. G. Fujimoto, "Femtosecond hot carrier energy relaxation in GaAs," Applied Physics Letters **51**, p. 1442 (1987).

[20]   C. J. Stanton, D. W. Bailey, and K. Hess, "Femtosecond-pump, continuum-probe nonlinear absorption in GaAs," Physical Review Letters **65**, p. 231 (1990).

[21]   W. H. Knox, C. Hirlimann, D. A. B. Miller, J. Shah, D. S. Chemla, and C. V. Shank, "Femtosecond excitation of nonthermal carrier populations in GaAs quantum wells," Physical Review Letters **56**, p. 1191 (1986).

[22] W. H. Knox, D. S. Chemla, G. Livescu, J. E. Cunningham, and J. E. Henry, "Femtosecond carrier thermalization in dense fermi seas," Physical Review Letters **61**, p. 1290 (1988).

[23] P. C. Becker, H. L. Fragnito, C. H. Brito-Cruz, R. L. Fork, J. E. Cunningham, J. E. Henry, and C. V. Shank, "Femtosecond photon echoes from band-to-band transitions in GaAs," Physical Review Letters **61**, p. 1647 (1988).

[24] S. Das Sarma, J. K. Jain, and R. Jalabert, Physical Review B **37**, p. 6290 (1988).

[25] P. C. Becker, H. L. Fragnito, C. H. Brito-Cruz, J. Shah, R. L. Fork, J. E. Cunningham, J. E. Henry, and C. V. Shank, "Femtosecond intervalley scattering in GaAs," Applied Physics Letters **53**, p. 2089 (1988).

[26] J. Y. Bigot, M. T. Portella, R. W. Schoenlein, J. E. Cunningham, and C. V. Shank, "Resonant intervalley scattering in GaAs," Physical Review Letters **65**, p. 3429 (1990).

[27] Y. H. Lee, A. Chavez-Pirson, S. W. Koch, H. M. Gibbs, S. H. Park, J. Morhange, A. Jeffery, N. Peyghambarian, L. Banyai, A. C. Gossard, and W. Wiegmann, "Room temperature optical nonliearities in GaAs," Physical Review Letters **57**, p. 2446 (1986).

[28] K. Meissner, B. Fluegel, H. Giessen, B. P. McGinnis, A. Paul, R. Binder, S. W. Koch, N. Peyghambarian, M. Grun, and C. Klingshirn, "Spectral hole burning in the gain region of an inverted semiconductor," Physical Review B **48**, p. 15472, (1993).

[29] H. Frohlich, Proceedings of the Royal Society A (London) **188**, p. 532 (1947).

[30] R. Stratton, "The influence of interelectronic collisions on conduction and breakedown in polar crystals," Proceedings of the Royal Society A (London) **246**, p. 406 (1958).

[31] D. K. Ferry, "First order optical and intervalley scattering in semiconductors," Physical Review B **14**, p. 1605 (1976).

[32] M. A. Littlejohn, J. R. Hauser, and T. H. Glisson, "Velocity-field characteristics of GaAs with Γ-L-X conduction band ordering," Journal of Applied Physics **48**, p. 4587 (1977).

[33] J. D. Wiley, "Polar mobility of holes in III-V compounds," Physical Revew B **4**, p. 2485 (1971).

[34] M. Costato and L. Reggiani, "Scattering probabilities for holes I.: Deformation potential and ionized impurity scattering," Phys. Stat. Sol. B **58**, p. 471 (1973).

[35] M. Costato and L. Reggiani, "Scattering probabilities for holes II.: Polar optical scattering mechanism," Phys. Stat. Sol. B **58**, p. 47 (1973).

[36] S. Zollner, S. Gopalan, and M. Cardona, "Intervalley deformation potentials and scattering rates in zinc blende semiconductors," Applied Physics Letters **54**, p. 614 (1989).

[37] M. Lindberg and S. W. Koch, Physical Review B **38**, p. 3342 (1988).

[38] H. Haug and S. W. Koch, Quantum theory of the optical and electronic properties of semiconductors, World Scientific, Singapore, 1993.

[39] A. Knorr, R. Binder, E. M. Wright, and S. W. Koch, "Amplification, absorption, and lossless propagation of femtosecond pulses in semiconductor amplifiers," Optics Letters **18**, p. 1538 (1993).

[40] T. Kurosawa, Journal of the Physical Society of Japan Supplement **21**, p. 424 (1966).

[41]   W. Fawcett, A. D. Boardman, and S. Swain, "Monte Carlo determination of electron transport properties in gallium arsenide," Journal of Physics and Chemistry of Solids **31**, p. 1963 (1970).

[42]   M. A. Osman and D. K. Ferry, "Monte Carlo investigation of the electron-hole-interaction effects on the ultrafast relaxation of hot photoexcited carriers in GaAs," Physical Review B **36**, p. 6018 (1987).

[43]   L. Rota and D. K. Ferry, "Monte Carlo investigation of carrier-carrier effects in femtosecond pump and probe experiments," Applied Physics Letters **62**, p. 2883 (1993).

[44]   C. Jacoboni and L. Reggiani, "The Monte Carlo method for the solution of charge transport in semiconductors with applications to covalent materials," Reviews of Modern Physics **55**, p. 645 (1983).

[45]   P. Lugli, C. Jacoboni, and L. Reggiani, "Monte Carlo algorithm for hot phonons in polar semiconductors," Applied Physics Letters **50**, p. 1251 (1987).

[46]   K. Brennan and K. Hess, "Theory of high field transport of holes in GaAs and InP," Physical Review B **29**, p. 5581 (1984).

[47]   C. J. Stanton, D. W. Bailey, and K. Hess, "Monte Carlo modeling of femtosecond relaxation processes in AlGaAs/GaAs quantum wells," IEEE Journal of Quantum Electronics **24**, p. 1614 (1988).

[48]   C. J. Stanton and D. W. Bailey, "Evaluating photoexcitation experiments using Monte Carlo simulations," in Monte Carlo Simulations of Semiconductors and Semiconductor Devices, edited by K. Hess, Kluwer Academic, 1993.

[49]   C. J. Stanton, private communication.

Chapter 3
Femtosecond laser system

3.0 Introduction

We use a variety of femtosecond lasers, amplifiers, and nonlinear optical processes to generate femtosecond light pulses for experiments. In fact, a large portion of our time in the lab is spent building or tweaking lasers. This stems partly from the philosophy that state-of-the-art laser technology will enable us to make measurements that are inaccessible to other researchers, and therefore guaranteed to be new and interesting. This strategy has worked hansomely in the past. With the proliferation of femtosecond technology, and in particular modelocked Ti:Sapphire lasers, the strategy is not on as firm footing as it once was.

In this chapter we describe the femtosecond laser system that was used to perform the experiments described in chapters 5 and 6. The system consists of a femtosecond oscillator amplified by a copper vapor laser pumped dye amplifier. The amplified femtosecond pulses that the system produces are modified by various linear and nonlinear optical techniques before being used in pump-probe absorption saturation spectroscopy.

3.1 CPM
3.1.1 Design

The source of femtosecond laser pulses used for all the experiments described in this thesis is a home-built, colliding pulse modelocked (CPM) ring dye laser. The CPM was invented in 1981 by

Fork, Greene, and Shank at AT&T Bell Laboratories [1]. It quickly became the standard source for femtosecond laser pulses in laboratories around the world. For 11 years after its invention the CPM held the distinction of generating the shortest optical pulses of any laser.

Fig. 3.1 CPM Laser
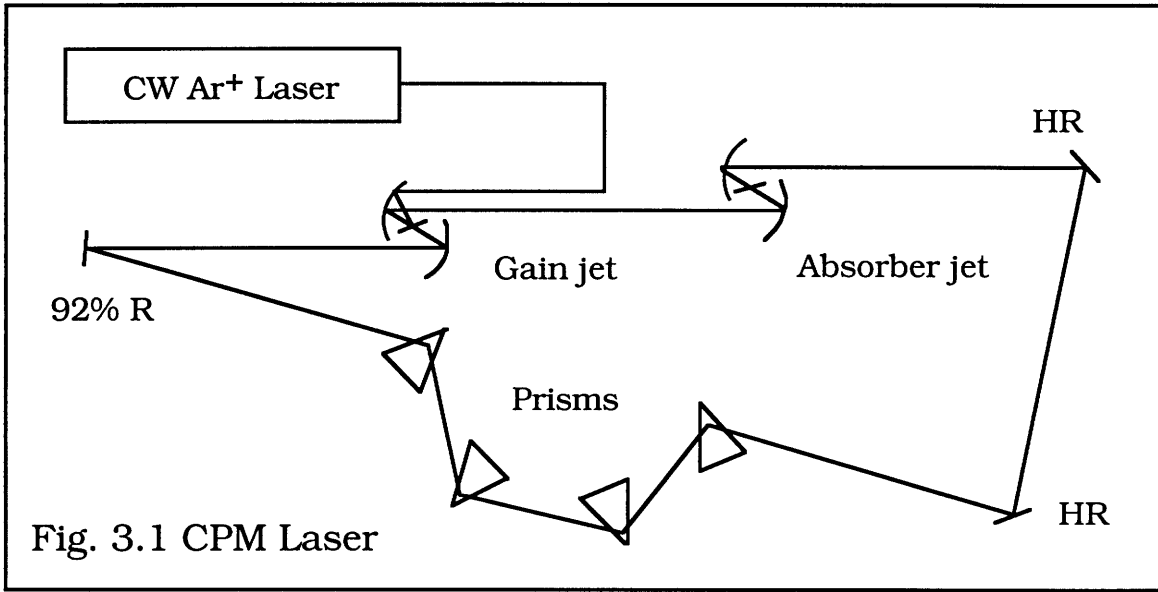
The CPM cavity [Figure 3.1] usually consists of seven mirrors although some six mirror CPM's have been built. One pair of curved mirrors forms a beam waist in the Rhodamine 6G (also called Rhodamine 590) gain dye jet while the other pair focusses the beam in the DODCI absorber dye jet. The remaining three mirrors are flat and serve to steer the beam around the ring. One of the flat mirrors is an 8% transmitting output coupler.

It is sometimes argued that seven mirror cavities are superior to those with six because the odd number of reflections leads to more uniform beam quality. In the six mirror cavity, however, flat mirror performance may be better optimized near normal incidence. It is probably easier to tweak a seven mirror CPM since the extra reflector helps decouple curved and flat mirror alignment. Our CPM uses the seven mirror design.

26

The curved mirrors must be placed so that the astigmatism inherent in using them off normal incidence compensates for the astigmatism caused by focussing the beam through the tilted cross section of the dye jet [2]. The radius of curvature of the mirrors surrounding the gain dye jet is 10 cm; around the absorber it is 5 cm. The mirrors are placed so that the spot in the absorber is smaller than that in the gain. All of the mirrors, including the flats, are dielectric multistack reflectors.

The beam also passes through four fused silica prisms which are included in a geometry that provides negative group velocity dispersion [3]. Each prism intercepts the beam at Brewster's angle for minimum loss. The prisms are arranged in two pairs so that the spread of wavelengths across the beam caused by the first pair is exactly cancelled by the second pair.

The theory of CPM operation is well established [4]. We briefly rewiew only the main principles here. The CPM is a passively modelocked laser meaning that there are no externally driven modulators or modelockers present. It is modelocked by a slow (compared to the pulse width) saturable absorber which has the important qualities of saturating more easily and recovering more quickly than the gain. These saturation characteristics allow a pulse propagating in the cavity to create its own window of net gain during the time between when the absorber saturates and when the gain saturates soon afterward. The saturation of the absorber is enhanced by the effect of two counter propagating pulses colliding in the absorber jet. The collision of the two pulses leads to an effectively larger absorber cross section which enhances the effects of passive modelocking.

Once established, the pulses in the CPM cavity undergo pulse shaping that is the result of the balance between four competing mechanisms. The pulse is shaped by the saturable gain, the saturable loss, self phase modulation, and group velocity dispersion compensation. The saturable gain and loss sharpen the trailing and leading edges of the pulse respectively. Self phase modulation occurs when the intracavity beam is focussed tightly in the abosrber jet. It comes from the intensity dependent index of refraction of the ethylene glycol in which the absorber dye is dissolved. Because the index varies with intensity and the intensity of the pulse varies in time, the pulse experiences a time dependent phase shift as it passes through the jet. This phase shift leads to the generation of new frequencies in the pulse. The chirp from self phase modulation is compensated by the prisms which act together as an optical element with negative group velocity dispersion. These four processes continue to shorten the pulse until some other nonlinearity imposes a limit. This limit may come from the bandwidth of the dyes, the mirrors, and from third or higher order dispersion in the prisms.

Our CPM performs near the limits reported in the literature [4] which is significantly better than average according to visitors to our lab. We have observed stable pulses as short as 30 fs and routinely achieve durations of 50 fs. Each of the two output beams delivers 20 mW average power which corresponds to 0.2 nJ per pulse at 100 MHz repetition rate. The peak power of each pulse is approximately 4 kW. The center wavelength of the laser is 625 nm.

3.1.2. Brief operating hints

Our CPM is pumped by a Spectra-Physics 2030-15T argon ion laser. The argon laser is the limiting factor in CPM stability over a period of several hours. The argon laser slowly drifts out of alignment causing the power to drop and the beam direction to change slightly. These problems are the greatest during the first hour of operation and at any time when the air temperature in the lab is changing. The newer generation of stablilzed argon lasers offer improved performance.

After the basic alignment of the CPM is complete [4], performance is maximized primarily through two controls: movement of the absorber dye jet in and out of the beam focus and insertion of prism glass into the beam. As the absorber dye jet is moved closer to the focus the dye is saturated more and self phase modulation increases. The saturable absorption is balanced against the saturable gain in the gain jet while the self phase modulation is compensated by negative group velocity dispersion in the prisms. The prisms are placed in a configuration that produces negative group velocity dispersion. As any prism is inserted into the beam along its apex bisector, the amount of glass through which the beam propagates is increased and the dispersion becomes less negative. The usual optimization procedure is therefore to back the prisms out of the beam until it just passes through the tips. The absorber jet is then translated to a position near, but usually not at, the point of maximum output bandwidth. Finally the prisms are inserted to shorten the pulse as much as possible but not so much that the laser becomes unstable.

The gain dye, Rhodamine 6G, is relatively easy to use, dissolves well in ethylene glycol, lasts for many months, and does not need to be filtered for dust as the gain jet nozzle is about 300 um wide. Rhodamine

6G is also called Rhodamine 590 and comes in chloride and tetrafluoroborate forms both of which seem to work equally well. The absorber, DODCI, degrades in solution within as little as ten days after preparation. It does not dissolve in ethylene glycol as easily as Rhodamine does and it has to be filtered because the 50 to 100 um wide jet nozzle clogs easily. We have found that an absorber jet as thick as 100 to 125 um is advantageous because it allows us to use lower concentrations of DODCI which can last as long as six weeks. We also keep the DODCI refrigerated, following a suggestion from researchers at AT&T.

## 3.2 CVL pumped dye amplifier
3.2.1 Design

The wavelength of CPM pulses is determined by the dyes and the mirrors in the laser and is not tunable. Some researchers have used different dyes and mirror sets to build CPM's at other visible and infrared wavelengths [5]. None of these other wavelength CPM's has matched the Rhodamine 6G - DODCI combination in pulse shortness. Femtosecond white light continuum generation is one way to generate femtosecond optical pulses at wavelengths besides the CPM center wavelength.

In order to generate a continuum or use other high intensity nonlinear optical effects it is neccessary to amplify the CPM pulses. We use a copper vapor laser (CVL) pumped dye amplifier to increase the intensity of the CPM pulses by a factor of about 10,000. In order to achieve this increase in pulse energy we are forced to trade off the repetition rate of the system down to 8 kHz. Thus the average power of

the beam at the output of the amplifier is actually lower than that at the input.

Our amplifier employs a two stage design [Figure 3.2].

Fig. 3.2
Dye Amplifier
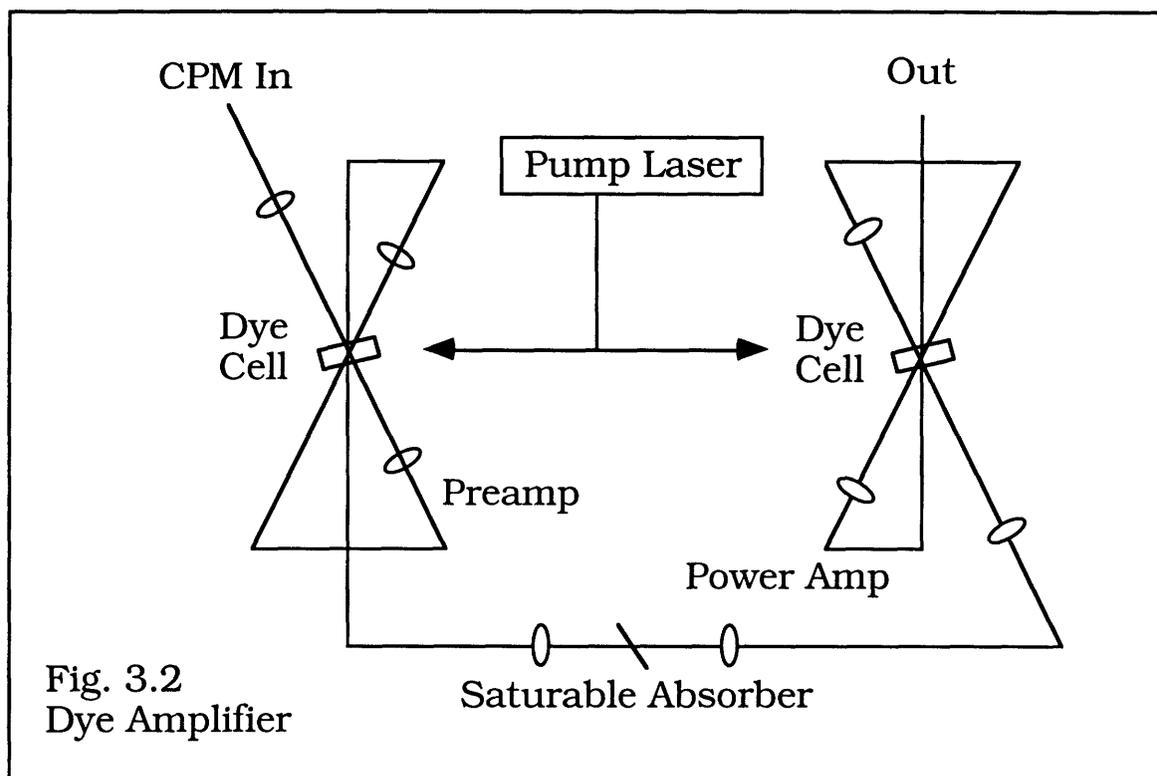
The first stage is optimized as a high gain preamplifier while the second is a high energy extraction power amplifier.

At the heart of the amplifier are two glass cells which channel a 2 mm thick flowing stream of Sulfarhodamine 640 gain dye. The first stage of the amplifier consists of lenses and mirrors arranged to focus the CPM beam through the cell three times. On the first pass the waist size in the cell is about 10 um. A relay imaging system is used to increase the spot size by a factor of 3 on each pass in order to reduce saturation effects. The spot size of the CVL pump beam is about 300 um. The pump spot must be significantly bigger than any one of the wasits of the beam being amplified because it transits the cell at different angles on each pass.

The second stage design is similar to that of the first stage except that the spots are much larger (pump 1000 um, CPM beam 100 - 900 um). The amplifier is highly saturated in the second stage for maximum energy extraction and also to reduce intensity fluctuations in the ouput.

An early version of the amplifier [6] used large core multimode optical fibers to deliver the pump light from the CVL to the gain dye cells. This method had the advantages that the fiber homogenized the spiky spatial profile of the CVL output beam, some table space was saved, and the output end of the fiber could be imaged on the dye cell to form a uniform gain volume. A 400 um core diameter fiber was used to pump the first stage while a 1000 um core diameter was used for the second. The bright green glow of the fibers was quite beautiful in the lab. The main disadvantages were that the input face of the fibers often burned and only about 60 % of the incident light could be recovered at the other end. Also the input end of the fiber could not be mounted closer than approximately one CVL cavity length from the CVL output coupler or else reflections were coupled back into the CVL, suppressing its output. It was for all these reasons that we eventually decided to abandon the fiber approach in favor of direct pumping by propagating the beam across the optical table to a lens and steering mirror near each cell. The 20 W CVL beam is 2.5 cm in diameter so it must be covered as it travels so that air currents do not cause ripples in the beam profile.

For good amplifier performance it is essential to reduce amplified spontaneous emission. We use four techniques to this end. First, it has been shown [7] that a long, thin gain volume is preferable to a short, fat one. In the long, thin geometry there are simply fewer directions for ASE to amplified. In our amplifier the ratio of the length of the gain volume to

its diameter is 5:1 to 10:1. Second, we had the outside of the cells antireflection coated at 625 nm to prevent the cell from lasing. Third, we tilted the cells so that the entrance and exit spots of the pump beam on the cell faces are not opposite each other. Finally, a jet of Malachite Green saturable absorber is placed between the first and second stages. The amplified beam is focussed into the saturable absorber so that the pulses are attenuated by a factor of two while the linear transmission is about one percent.

We use a home built electronic synchronizer to fire the CVL in sync with the CPM. The circuit is based on a monostable multivibrator oscillator and two D flip flops. It is implemented in emitter coupled logic chips because the CPM's 100 MHz repetition rate is close to the speed limit for normal transistor transistor logic. The circuit essentially triggers the CVL thyratron at 8 kHz modulo the CPM interpulse arrival time of about 10 ns. It does not compensate for jitter in the CVL thyratron which can be a problem at times.

When the amplifier was first built we demonstrated an additional feature that was later abandoned. We found that there was sufficient pulse energy after only one stage of amplification that the beam could be focussed into a cell of flowing water and a broad spectrum could be generated. We used an interference filter to select out light in the near infrared and reamplified that light with a different dye, LDS821, in the second stage. Investigators at Lawrence Berkeley Laboratory have used a similar design with an excimer pump laser to generate femtosecond blue pulses [8].

Two prisms in a double pass sequence are set up after the amplifier to compensate for group velocity dispersion. With the prisms it is possible to obtain 70 fs pulses with pulse energies as high as 5 uJ.

3.2.2 Brief operating hints

The copper vapor laser provides the best performance of any pump laser suitable for femtosecond pulse amplification. It can deliver 2 mJ green pulses that are 15 ns long at repetition rates as high as 10 kHz. Its use in femtosecond pulse amplification [9] revolutionized ultrafast spectroscopy. The CVL's main competitors are Q-switched, frequency doubled Nd:YAG and Nd:YLF lasers many of which only offer 1 kHz repetition rates and either low power or pulses too long to be useful. Despite these shortcomings we have recently switched to a diode pumped, Q-switched, frequency doubled Nd:YLF laser to pump our amplifier.

Most of the time the CVL (Metalaser 2051) does not work at its specified output power. And no matter what power is obtained, the warm up and temperature stabilization time is typically 4 to 6 hours. Common failure modes of the CVL are thyratron failure, plasma tube cracking, and several types of electronic failures. It's useful to have a complete list of third party sources for CVL components since the manufacturer has discontinued scientific sales and support.

We now use a Spectra-Physics TFR diode pumped, Q-switched, frequency doubled Nd:YLF laser to pump our dye amplifier. TFR denotes the tightly folded resonator design used in the laser cavity. The TFR generates 200 uJ, 6 ns long, green pulses at 1 kHz. Although the average power is 100 times less than that of a CVL operating at spec, the

TFR is far more useful than its predecessor. It has a ten minute warm up time, is perfectly stable and generates a clean spatial mode which may be efficiently focussed into the amplifier dye cells.

3.3 Continuum generation

One of the most important uses of the femtosecond amplifier is to create pulses that are intense enough to generate a white light continuum when focused into an appropriate transparent medium [10]. Continuum generation is the result of extreme self phase modulation of an ultrashort light pulse.

An intense femtosecond laser pulse endures self phase modulation upon propagation through a transparent medium because the index of refraction is an intensity dependent quantity:

$$n = n_0 + n_2 I + ...$$ (1)

Since the intensity of a femtosecond pulse is a rapidly varying function of time, the pulse will experience a time dependent phase shift. The instantaneous frequency of the optical field is the time derivative of the phase so the time dependent phase shift will generate new frequencies in the pulse. The amount of spectral broadening is proportional to the peak intensity.

In practice, to generate a continuum we focus an amplified femtosecond laser beam into a 1 mm thick flowing jet of ethylene glycol. The beam changes color from red to white. The spectrum of the continuum extends from approximately 400 nm to beyond 800 nm. The power drops off rapidly as a function of detuning from the wavelength of the input beam.

3.4 Cavity dumped Ti:sapphire laser

W. Knox has pointed out that most femtosecond laser systems produce average powers of about 10 mW. [11] There is a trade off between pulse energy and repetition rate. In round numbers, for example, the CPM produces 0.1 nJ pulses at 100 MHz while a four stage dye amplifier pumped by a Q-switched Nd:YAG laser may generate 500 mJ pulses at 20 Hz. These systems represent extremes for most experiments investigating femtosecond phenomena in solid state materials and devices. The copper vapor laser pumped dye amplifier fills in the gap at 1 uJ and 10 kHz. Still, for many applications 0.1 uJ at 100 kHz would be better because of better signal averaging and lockin detection at high repetition rates.

We have constructed a Kerr lens modelocked, cavity dumped Ti:Sapphire laser in an effort to obtain high pulse energies at repetition rates as high as hundreds of kilohertz [Figure 3.3].
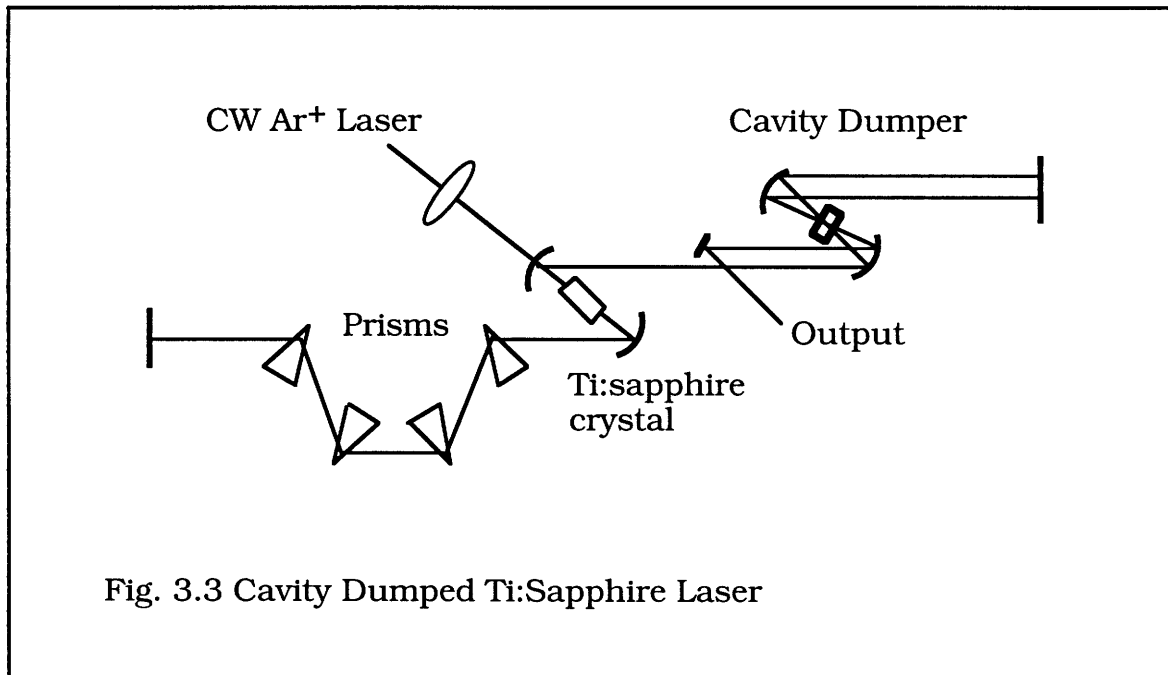

Fig. 3.3 Cavity Dumped Ti:Sapphire Laser

The laser is similar to other modelocked Ti:Sapphire lasers [12] with the

addition of an additional intracavity fold designed to focus the laser beam into an acoustooptic cavity dumper.

The acoustooptic cavity dumper is a 2.5 mm thick quartz cell inserted at Brewster's angle between two 10 cm radius of curvature mirrors. The diffracted beam makes two passes through the cell and is picked off by a small mirror close to the intracavity beam. The total diffraction efficiency is 60 %.

We obtained 0.1 uJ dumped output pulses as short as 50 fs at repetition rates as high as 952 kHz. The repetition rate could be reduced to various submultiples of the inverse cavity round trip time with similar pulsewidth and energy performance. Cavity dumping is nonresonant and broadband and therefore preserves the spectral and temporal performance of a conventional femtosecond Ti:Sapphire laser. Recently our technique has been repeated by others who report 15 fs, 60 nJ pulses [13]. We anticipate that this laser will be a valuable source for femtosecond nonlinear optical experiments in the near future.

3.5 Conclusion

Our arsenal of femtosecond lasers is large and constantly evolving. It is not a bold prediction to say that in the next few years femtosecond laser pulses will be available across most of the optical spectrum. In the future the experimentalist will have access to any desired spectral window and transform limited pulses to which it corresponds.

For the experiments described in this thesis we have used a colliding pulse modelocked laser amplified by a copper vapor laser pumped two stage dye amplifier. In some of the experiments we use continuum generation techniques to access wavelengths other than the

CPM center wavelength. A cavity dumped Ti:Sapphire laser has been constructed in an effort to create a laser with a combination of pulse energy and repetition rate most desirable for nonlinear optical experiments.

3.6 References

[1]   R. L. Fork, B. I. Greene, and C. V. Shank, "Generation of optical pulses shorter than 0.1 psec by colliding pulse mode locking," Applied Physics Letters, **38**, p. 671-672 (1981)

[2]   H. W. Kogelnik, E. P. Ippen, A. Dienes, and C. V. Shank, "Astigmatically compensated cavities for cw dye lasers," IEEE Journal of Quantum Electronics **8**, p. 373 (1972).

[3]   R. L. Fork, O. E. Martinez, and J. P. Gordon, "Negative dispersion using pairs of prisms," Optics Letters **9**, p. 150 (1984).

[4]   J. A. Valdmanis, R. L. Fork, and J. P. Gordon, "Generation of optical pulses as short as 27 femtoseconds directly from a laser balancing self-phase modulation, group-velocity dispersion, saturable absorption, and saturable gain," Optics Letters, **10**, p. 131-133 (1985).

[5]   P. Georges, F. Salin, G. LeSaux, G. Roger, and A. Brun, "Femtosecond pulses at 800 nm by passive mode locking of Rhodamine 700," Optics Letters, **15**, p. 446-448 (1990).

[6]   M. Ulman, R. W. Schoenlein, and J. G. Fujimoto, Technical Digest of the OSA Annual Meeting (Optical Society of America, Washington, DC, 1989).

[7]   D. Nickel, D. Kuhlke, and D. von der Linde, "Multipass dye-cell amplifier for high-repetition-rate femtosecond optical pulses," Optics Letters, **14**, p. 36-38 (1989).

[8]   R. W. Schoenlein, J. Y. Bigot, M. T. Portella, and C. V. Shank, "Generation of blue-green 10 fs pulses using an excimer pumped dye amplifier," Applied Physics Letters, **58**, p. 801-803 (1991)

[9]   W. H. Knox, M. C. Downer, R. L. Fork, and C. V. Shank, "Amplified femtosecond optical pulses and continuum generation at 5 kHz repetition rate," Optics Letters, **9**, p. 552-554 (1984).

[10]   R. L. Fork, C. V. Shank, C. Hirlimann, R. Yen, and W. J. Tomlinson, "Femtosecond white-light continuum pulses," Optics Letters, **8**, p. 1-3 (1983).

[11]   W. H. Knox, "Femtosecond optical pulse amplification," IEEE Journal of Quantum Electronics, **QE-24**, p. 388-397 (1988).

[12]   M. Ramaswamy, M. Ulman, J. Paye, and J. G. Fujimoto, "Cavity dumped femtosecond Kerr lens modelocked Ti:Al$_2$O$_3$ laser," Optics Letters **18**, p. 1822 (1993).

[13]   M. S. Pshenichnikov, W. P. de Boeij, and D. A. Wiersma, "Generation of 13 fs, 5 MW pulses from a cavity dumped Ti:sapphire laser," Optics Letters **19**, p. 572 (1994).

Chapter 4
Theory and simulation of femtosecond carrier dynamics in AlGaAs

4.0 Introduction

The data from femtosecond pump-probe experiments look deceptively simple. In a typical differential transmission experiment, for example, the data show a fast bleaching of the sample by the pump pulse followed by recovery. It is relatively easy to deconvolve an exponential time constant from the data and thereby quote a response time. For phenomenological work this approach is perfectly adequate, and in some engineering applications more detail could actually be a burden, not a benefit. It is the dynamics of hot carriers, however, that fundamentally determine the optical response. These dynamics are not easily extracted from pump-probe data.

In this chapter we point out the essential features of a method for theoretically predicting the dynamics of hot carriers in AlGaAs on a femtosecond time scale. The goal is to determine the carrier distributions as a function of position, momentum, and time. The theoretical results will be compared to experiment in Chapter 5 where we compare simulated pump-probe data to actual data. Much of the analysis presented here may be found in references such as the comprehensive review article by Jacaboni and Reggiani [1], and the books by Lundstrom [2] and Ridley[3].

The procedure we use is based on three steps: calculation of realistic bandstructures and scattering rates, solution of the Boltzmann

transport equation by ensemble Monte Carlo simulation, and prediction of absorption saturation data. It is necessary to use Monte Carlo simulation rather than an analytic procedure because the simulation is the only practical way to include a large number of the details which must be considered. Monte Carlo allows us to account for effects from a variety of scattering mechanisms, nonparabolic bands, and multiple optical transitions, for example.

The bandstructure calculations, the Monte Carlo simulations, and the nonlinear absorption calculations were performed by Prof. D. W. Bailey of the University of South Carolina and Prof. C. J. Stanton of the University of Florida.

4.1 Bandstructure

The first step in performing an accurate simulation of hot carrier dynamics in a semiconductor is the calculation of a realistic bandstructure. Knowledge of the proper bandstructure is essential for the calculation of scattering rates as shown in the next section. We use a perturbative technique, the k•p method, to perform bandstructure calculations. This method is most accurate near the zone center which is where most of the hot carriers in our experiments reside. The k•p method is also computationally efficient which makes it an attractive choice. It is faster than the empirical pseudopotential method, for example.

4.1.1 Explanation of the k•p method

There are many experiments including optical absorption and cyclotron resonance that are able to elucidate the energies of the basis

states in a semiconductor at k=0. We take the k=0 energy levels as given, either from experiment or from previous work [4]. The k=0 Bloch functions are a complete set of periodic functions and therefore it is possible to expand the periodic part of the wave function at any k in terms of the k=0 wavefunctions. A diagonalized k•p Hamiltonian should give accurate energy bands for any point in the Brillouin zone if enough k=0 basis states are used [4][5].

The k•p Hamiltonian comes from substituting the Bloch functions,

$$\Psi = e^{i\vec{k}\cdot\vec{r}}u_{n,k}(\vec{r}) \tag{1}$$

into the Schroedinger equation to get:

$$\left\{\frac{p^2}{2m} + \frac{\hbar}{m}\vec{k}\cdot\vec{p} + \frac{\hbar^2\vec{k}^2}{2m}\right\}u_{n,\vec{k}} = E_{n,\vec{k}}u_{n,\vec{k}} \tag{2}$$

The energy to first order in perturbation theory is

$$E_{n,\vec{k}} = E_{n,0} + \frac{\hbar}{m}\vec{k}\cdot\langle n0|\vec{p}|n0\rangle. \tag{3}$$

The k•p Hamiltonian is diagonal at k=0 but not at $k \neq 0$ because of the k•p term. When $k \neq 0$ we need to find the matrix elements of p between our basis states and then diagonalize the matrix. Interestingly, we never need to know what the k=0 wavefunctions are, although we do use their symmetry properties. We determine the matrix elements of p to within constant fitting factors by considering the symmetries of the various basis states involved. The fitting factors are close to those used in [4] and are listed in [6].

The k•p Hamiltonian is a 30 x 30 matrix. This comes from 15 basis states times 2 for spin. The 15 states are as follows [9]:

Irreducible Rep.	Atomic State	Plane Wave	Energy (Ry)	Basis Functions
Γ_1^l	s+	[000]	-0.966	1

$\Gamma_{25'}^{l}$	p+	[111]	0.00	X=yz; Y=xz; Z=xy
$\Gamma_{2'}^{l}$	s-	[111]	0.0728	xyz
Γ_{15}	p-	[111]	0.232	x; y; z
Γ_{1}^{u}	s+	[111]	0.571	1
$\Gamma_{12'}$	d-	[200]	0.771	$3z^2 - r^2; \sqrt{3}(x^2 - y^2)$
$\Gamma_{25'}^{u}$	d+	[200]	1.25	X=yz; Y=xz; Z=xy
$\Gamma_{2'}^{u}$	s-	[200]	1.35	xyz

When we use Fermi's Golden Rule to calculate scattering rates we have to find matrix elements of the scattering potential. Since the electron wavefunctions are Bloch states, the integral separates into $\langle u_k | u_{k'} \rangle U(k - k')$ where the $|u_k\rangle$ are the periodic part of the wavefunctions and $U(k - k')$ is the scattering potential integrated between plane wave states. The k•p wavefunctions are linear combinations of the k=0 wavefunctions, $|u_{n,\bar{k}}\rangle = \sum_{n'} c_{n'}^{n}(\bar{k})|n'\rangle$ where the c's are the elements of the eigenvectors from diagonalizing the k•p Hamiltonian. Since the k=0 states $|n\rangle$ are orthonormal, we don't need to know explicitly what they are. The integrals $\langle u_{\bar{k}} | u_{\bar{k}'} \rangle$ are the Bloch overlap factors (discussed further in 4.2.2).

The k•p method is also convenient in that it takes care of most of the work of calculating the optical matrix elements. In the dipole approximation the optical matrix element is calculated from the substitution $\dfrac{p^2}{2m} \to \dfrac{\left(\bar{p} - \dfrac{e\bar{A}}{c}\right)^2}{2m}$ so we need matrix elements of p. We already know these from the k•p calculation. We use the semiclassical

approximation in which A is not an operator and we ignore the A^2 term which is small.

4.1.2 Bandstructure calculations

We use the effective mass approximation for electrons in a three valley model for the conduction band. The Γ valley is considered to be isotropic and nonparabolic. The nonparabolicity constant, α, is 0.64 eV^{-1} in the expression

$$E(1+\alpha E) = \frac{\hbar^2 k^2}{2m^*} \tag{4}$$

The effective mass approximation is not valid for holes over the range of energies that occur in our experiments. Hole band warping and anisotropy must be included for accurate results. The heavy hole, light hole, and split off hole bands are calculated using the k•p procedure just described [4][5].

In Fermi's Golden Rule the transition rate is proportional to the density of final states. The density of states, $g_v(E)$, is used in intraband processes such as scattering rates while the joint density of states, $\rho_v(E)$, is used to calculate nonlinear absorption. In the effective mass approximation the density of states is $g_v(E)dE = \frac{1}{\pi^2}\left(\frac{m^*}{\hbar}\right)^{3/2}\sqrt{2E}dE$. The expression for the joint density of states is the same except $\mu = \left(\frac{1}{m_c^*} + \frac{1}{m_v^*}\right)^{-1}$ is substituted for m. The subscripts c and v refer to the conduction and valence bands. When the effective mass approximation in invalid, as is the case for the hole bands, we calculate $g_v(E)$ and $\rho_v(E)$ using

$$g_v(E)dE = \frac{1}{4\pi^3}\int_{S(E)}\frac{dS}{|\nabla_k E_v(k)|} \tag{5}$$

44

and

$$\rho_v(E)dE = \frac{1}{4\pi^3} \int_{S(E)} \frac{dS}{\left|\nabla_k\left(E_c(k) + E_v(k)\right)\right|} \tag{6}$$

where S(E) is an isoenergy surface in k space.

Finally the k•p method is used to calculate the Bloch overlap integrals (discussed in 4.2.2). The Bloch overlap integral is the inner product of the periodic part of the initial and final Bloch states. Wiley used a 4 band k•p method to determine Bloch overlap integrals, G, for light hole and heavy hole interactions [8]. He calculated

$$G_{lh-lh} = G_{hh-hh} = \frac{1}{4}\left(1 + 3\cos^2\theta\right) \tag{7}$$

$$G_{lh-hh} = G_{hh-lh} = \frac{3}{4}\sin^2\theta \tag{8}$$

where θ is the scattering angle for polar mode scattering.

Wiley's results are widely used, but are not sufficient in our case because they are a poor approximation at high energies and don't account for effects involving the split off band. We calculate Bloch overlap factors explicitly and implement them in Monte Carlo simulations using the rejection method. When a hole is selected for scattering, its final state and Bloch overlap integral are calculated. If the overlap integral is less than a random number uniformly distributed between 0 and 1, the scattering event is rejected.

4.1.3 Results: GaAs, $Al_xGa_{1-x}As$

Our calculated bandstructures for GaAs and $Al_{0.1}Ga_{0.9}As$ are shown in figures 4.1 and 4.2.

45
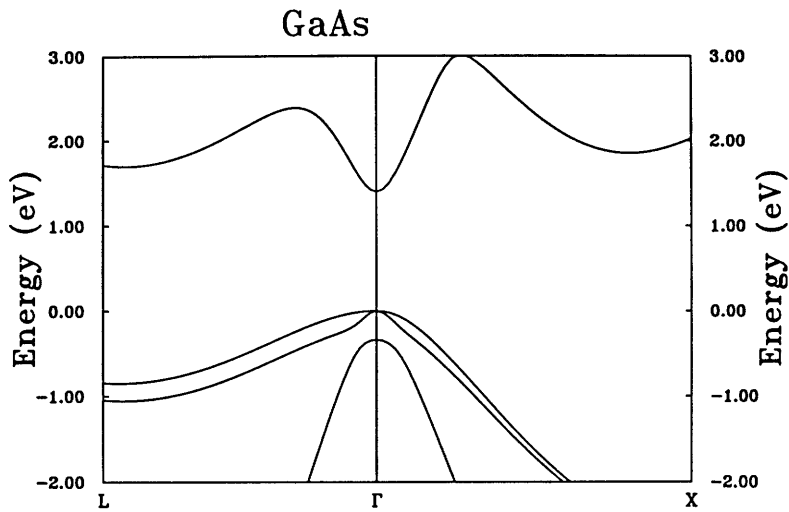
Fig. 4.1 Bandstructure of GaAs

The prominent features of the bandstructure are the three conduction band valleys Γ, L (<111> direction), and X (<100> direction), and the three valence hole bands. The hole bands come from p-like states: the heavy and light hole bands are the J=3/2 manifold (J=L$\oplus$S where L=1 and S=1/2) while the "split off" (L=0) band is the J=1/2 manifold.
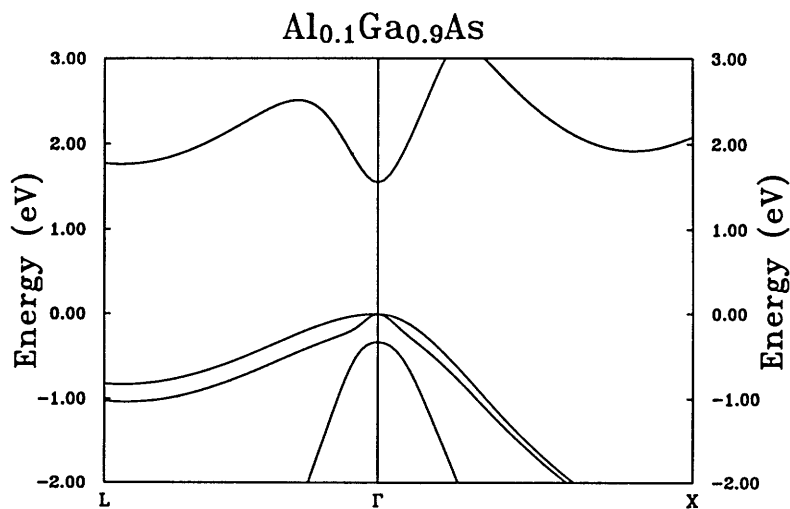

Fig. 4.2 Bandstructure of $Al_{0.1}Ga_{0.9}As$

It is interesting to note the nonparabolicity of the bands and that the dispersion is different in the L and X directions.

Figure 4.3 shows the heavy hole bandstructure near k=0. The large warping confirms our assertion that the effective mass approximation is invalid for the heavy hole band.
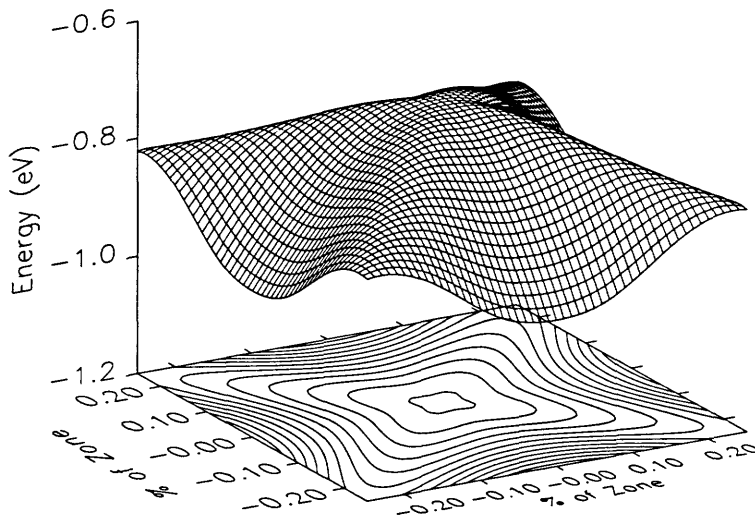

Fig. 4.3 Heavy hole warping.

4.2 Scattering rates

4.2.1 Discussion of possible scattering mechanisms

There are several possible scattering mechanisms that contribute to the relaxation dynamics of hot carrier distribution functions in semiconductors such as AlGaAs. They may be classified [1] as intravalley or intervalley for electrons and intraband or interband for holes. The causes of scattering are mainly phonons and other electrons.

Carriers interact with phonons via deformation potential scattering which occurs for both acoustic and optical phonons. Ionized impurities scatter electrons by the Coulomb interaction while the effect of neutral

impurities is so weak that they can be neglected. Carrier-carrier scattering is important at high carrier densities.

In our simulations polar optical phonon, deformation potential, electron-electron, electron-hole, and hole-hole scattering are included. All possible combinations of intrahole and interhole band scattering are taken into account. Acoustic phonons are only included in the simulation of interband scattering of holes. As shown below, carrier-carrier scattering rates depend on the carrier distributions and are therefore updated every 60 femtoseconds.

4.2.2 Simple calculation of various scattering rates

Considered one at a time, the individual scattering rates may be calculated relatively easily if certain details, such as realistic bandstructure, are ignored. We will illustrate the standard procedure here for ionized impurity scattering, polar optical phonon scattering, intervalley scattering, and carrier-carrier scattering [2][3]. We calculate scattering rates using Fermi's Golden Rule,

$$S(\text{p},\text{p}') = \frac{2\pi}{\hbar} \left| H_{p'p} \right|^2 \delta[E(p') - E(p) - \Delta E] \tag{9}$$

S is the transition rate from a state with momentum p to one with momentum p'. The matrix element of the interaction potential, U, is calculated as,

$$H_{p'p} = \int \psi_{p'}^* U \psi_p d^3x \tag{10}$$

When this is evaluated for Bloch waves one obtains

$$H(p',p) = I(p,p')U(p-p') \tag{11}$$

where

$$I(p,p') \equiv \int_{-\infty}^{\infty} u_p^*(x)u_{p'}(x)dx \tag{12}$$

48

is known as the Bloch overlap integral that was mentioned earlier and

$$U(p-p') = \int_{-\infty}^{\infty} e^{-ip'x} U(x,t) e^{ipx} dx.$$

(13)

For the calculations presented below we will assume a bandstructure with spherical constant energy surfaces and parabolic dispersion. In this case, the matrix element is just

$$H_{p'p} = \frac{1}{\Omega} \int e^{-ip \cdot r/\hbar} U(r) e^{ip \cdot r/\hbar} d^3 r$$

(14)

In the actual simulations which we compare to our experimental data a realistic bandstructure including heavy hole anisotropy and warping is used, so the Bloch overlap integrals are explicitly calculated [8].

From the transition rate we can calculate various relaxation times. The scattering rate is

$$\frac{1}{\tau(p)} = \sum_{p',\uparrow} S(p,p')$$

(15)

The momentum relaxation rate is

$$\frac{1}{\tau_m(p)} = \sum_{p',\uparrow} S(p,p')(1 - \frac{p'}{p}\cos\alpha)$$

(16)

where α is the angle between the incident and scattered momenta. The momentum relaxation rate measures the rate of momentum randomization for anisotropic scatterers. The energy relaxation rate,

$$\frac{1}{\tau_E(p)} = \sum_{p',\uparrow} S(p,p')(1 - \frac{E(p')}{E(p)})$$

(17)

indicates how quickly energy is dissipated in inelastic collisions.

4.2.2.1 Ionized impurity scattering

We will calculate the transition rate for ionized impurity scattering assuming that the scattering potential is a screened Coulomb potential given by

$$U(r) = \frac{q^2}{4\pi\kappa_s\varepsilon_0 r}e^{-r/L_D} \tag{18}$$

where the screening is characterized by the Debye length

$$L_D = \sqrt{\frac{\kappa_s\varepsilon_0 k_B T}{q^2 n_0}}. \tag{19}$$

Here, n_0 is the carrier density. The matrix element is

$$H_{p',p} = \frac{1}{\Omega}\left(\frac{q^2}{4\pi\kappa_s\varepsilon_0}\right)\int_0^{2\pi}\int_0^{\pi}\int_0^{\infty}e^{-r/L_D}e^{i(p-p')\cdot r/\hbar}r\sin\theta\, dr\, d\theta\, d\phi. \tag{20}$$

This may be integrated to find

$$H_{p',p} = \frac{-q^2}{\Omega\kappa_s\varepsilon_0}\frac{1}{(\beta/\hbar)^2 + 1/L_D^2}, \tag{21}$$

where β is the momentum change p-p'. Therefore the transition rate is given by

$$S(p,p') = \frac{2\pi N_I q^4}{\hbar\kappa_s^2\varepsilon_0^2\Omega}\frac{\delta(E'-E)}{\left[4\left(\frac{p}{\hbar}\right)^2\sin^2\left(\frac{\alpha}{2}\right) + \frac{1}{L_D^2}\right]^2} \tag{22}$$

where α is the angle between the initial and final momenta and N_I is the number of scatterers.

There are three regimes of screening depending upon the relative importance of the two terms in the denominator: weak, moderate, and strong. When screening is negligible, $L_D \to \infty$, and the transition rate is

$$S(p,p') = \frac{2\pi N_I q^4}{\hbar\kappa_s^2\varepsilon_0^2\Omega}\frac{\delta(E'-E)}{16\left(\frac{p}{\hbar}\right)^4\sin^4\left(\frac{\alpha}{2}\right)}. \tag{23}$$

On the other hand if screening is very strong, as is the case at high carrier densities, the transition rate becomes

$$S(p,p') = \frac{2\pi N_I q^4}{\hbar\kappa_s^2\varepsilon_0^2\Omega}\delta(E'-E). \tag{24}$$

In this case the scattering has the same form as that for a delta function potential. We see that the angular dependence of ionized impurity scattering is such that it scatters carriers by small angles unless it is

50

strongly screened, in which case it is isotropic. Ionized impurities are not a significant component of the actual scattering in our samples, but it is important to consider ionized impurity scattering because its mathematical form appears in other situations. For example, hole masses in GaAs are much greater than the electron masses so electron - hole scattering is treated as if holes were ionized impurities.

For the case of moderate screening we will evaluate the scattering rate as follows. The transition rate is integrated over all final states:

$$\frac{1}{\tau(p)} = \sum_{p',\uparrow} S(p,p') = \frac{\Omega}{(2\pi\hbar)^3} \int_0^{2\pi} \int_0^{\pi} \int_0^{\infty} \frac{2\pi N_I q^4}{\hbar \kappa_s^2 \varepsilon_0^2 \Omega} \frac{\delta(E-E')}{\left[4\left(\frac{p}{\hbar}\right)^2 \sin^2\left(\frac{\alpha}{2}\right) + \frac{1}{L_D^2}\right]^2} (p')^2 \sin\theta \, dp' \, d\theta \, d\phi \quad (25)$$

We define

$$\gamma^2 = 4L_D^2 \left(\frac{p}{\hbar}\right)^2 = 8mEL_D^2/\hbar^2 \quad (26)$$

and integrate over ϕ to obtain

$$\frac{1}{\tau(p)} = \frac{N_I q^4}{\kappa_s^2 \varepsilon_0^2} \frac{L_D^4}{2\pi\hbar^4} \int_0^{\infty} \delta(E-E)(p')^2 \, dp' \int_0^{\pi} \frac{\sin\theta \, d\theta}{\left[\gamma^2 \sin^2\left(\frac{\theta}{2}\right) + 1\right]^2} \quad (27)$$

The integral over θ is evaluated by the double substitution

$$x = \theta/2 \qquad dx = \frac{1}{2} d\theta$$

and

$$y = \gamma \sin x \qquad dy = \gamma \cos x \, dx$$

which leads to

$$\frac{4}{\gamma^2} \int_0^{\gamma} \frac{y \, dy}{\left(1+y^2\right)^2} = \frac{2}{\gamma^2 + 1}. \quad (28)$$

The p' integral is solved using

$$q = (p')^2 \qquad dq = 2p' \, dp'$$

so that one gets

$$\int_0^{\infty} \delta\left(\frac{q}{2m} - \frac{p^2}{2m}\right) \frac{1}{2} \sqrt{q} \, dq \quad (29)$$

51

which leads to the final result

$$\tau(p) = \frac{32\sqrt{2m}\pi\kappa_s^2\varepsilon_0^2}{N_I q^4} \frac{\left(1+\gamma^2\right)}{\gamma^4} E^{3/2}(p) \tag{30}$$

The momentum scattering time may be evaluated by calculating

$$\frac{1}{\tau_m(p)} = \frac{\Omega}{8\pi^3\hbar^3} \int\limits_0^{2\pi}\int\limits_{-1}^{1}\int\limits_0^{\infty} S(p,p')\left(1-\frac{p'}{p}\cos\alpha\right)p'^2\,dp'\,d(\cos\theta)d\phi \tag{31}$$

with the result

$$\tau_m(p) = \frac{16\sqrt{2m}\pi\kappa_s^2\varepsilon_0^2}{N_I q^4}\left[\ln\left(1+\gamma^2\right)-\frac{\gamma^2}{1+\gamma^2}\right]^{-1}E^{3/2}(p). \tag{32}$$

The procedure outlined above is known as the Brooks-Herring approach. Another method that is used is the Conwell-Weisskopf approach in which the unscreened potential is cut off at the mean distance between impurities, $b=\left[\dfrac{3}{4\pi n_I}\right]^{1/3}$. The Brooks-Herring formula is considered more appropriate [1] because it gives a scattering probability that decreases at high energies. This agrees with the fact that Coulomb scattering is strongly peaked in the forward direction for high energies.

The Born approximation, which underlies Fermi's Golden Rule, fails for slow moving electrons in a Coulomb potential [2]. Also we have not taken interference effects into account because we have calculated the scattering rates for a single impurity and multiplied by the number of impurities. Nevertheless, simple approaches, such as the Brooks-Herring method, give good physical insight into impurity scattering and are widely used.

4.2.2.2 Polar optical phonon scattering

GaAs is a polar semiconductor meaning that the bonds between the Ga and As atoms are partly ionic with the Ga atoms aquiring an effective negative charge and the As atoms a positive charge. Phonons

52

propagating in the crystal deform the lattice which changes the dipole moment between Ga and As atoms. Polar scattering refers to carriers which scatter off of the electric field from the perturbed dipole moment. The phonons responsible for polar scattering may be acoustic or optical. Polar acoustic phonon scattering is not important at room temperature, however, so we will ignore it. Polar optical phonon scattering is the primary mechanism by which hot electron distributions cool in GaAs. We present a simple calculation of the polar optical phonon scattering rate here.

The potential for polar optic phonon scattering is

$$U_{POP} = \frac{qq^*u}{i\beta V_u \varepsilon_0} \tag{33}$$

where q* is the effective charge of the dipole, u is the displacement, V is the volume of a unit cell, and β is the propagation constant of the acoustic wave. This is usually restated in terms of the high and low frequency dielectric constants by the substitution

$$\left[\frac{q^*}{V_u}\right]^2 = \frac{\varepsilon_0 \rho \omega_0^2}{\kappa_0}\left[\frac{\kappa_0}{\kappa_\infty} - 1\right]. \tag{34}$$

The transition rate is therefore

$$S(p,p') = \frac{\pi q^2 \omega_0}{\kappa_0 \varepsilon_0 \beta^2 \Omega}\left(\frac{\kappa_0}{\kappa_\infty} - 1\right)\left(N_0 + \tfrac{1}{2} \mp \tfrac{1}{2}\right)\delta(p' - p \mp \hbar\beta)\delta(E - E \mp \hbar\omega_0) \tag{35}$$

by Fermi's Golden Rule. The scattering rate is calculated by integrating the transition rate over all possible final states. This calculation differs from the case of ionized impurity scattering because it is necessary to take momentum conservation into account. The momentum conserving delta function dictates minimum and maximum phonon wavevectors that can participate in scattering. They are

$$\beta_{max} = \frac{p}{\hbar}\left[1 + \sqrt{1 \pm \frac{\hbar\omega_0}{E(p)}}\right] \quad \text{and} \quad \beta_{min} = \frac{p}{\hbar}\left[\mp 1 \pm \sqrt{1 \pm \frac{\hbar\omega_0}{E(p)}}\right]$$

The final result is

$$\frac{1}{\tau(p)} = \frac{q^2 \omega_0 \left(\frac{\kappa_0}{\kappa_\infty} - 1\right)}{2\pi\kappa_0\varepsilon_0\hbar\sqrt{2E(p)/m}} \left[N_0 \sinh^{-1}\left[\frac{E(p)}{\hbar\omega_0}\right]^{\frac{1}{2}} + (N_0 + 1)\sinh^{-1}\left[\frac{E(p)}{\hbar\omega_0} - 1\right]^{\frac{1}{2}} \right] \qquad (36)$$

As a function of energy the polar optic phonon scattering rate turns on sharply at the polar optic phonon energy and then flattens out at high energies. The rate is plotted versus energy in [2].

4.2.2.3 Intervalley scattering

In the usual treatment of intervalley scattering several possible phonon scattering channels are lumped together into a single intervalley deformation potential, D. In the experiments described in the next two chapters we are often concerned with electrons scattering between the Γ valley and the L satellite valley. For high photon energies it is also possible to photoexcite carriers which scatter to the X satellite valley. Intervalley scattering is an important effect in the dynamics of hot carriers in AlGaAs because there is a large number of states for carriers to scatter into in the satellite valleys. The satellite valleys have high effective masses; this coupled with intervalley scattering leads to negative differential resistivity and the Gunn effect.

The potential for Γ to L intervalley scattering is

$$U = D_{\Gamma L} u(x,t) \qquad (37)$$

The displacement, u, is treated as a quantum mechanical harmonic oscillator with the result that the transition rate becomes

$$S(p,p') = \frac{\pi D_{\Gamma L}^2 Z_L}{\rho\omega_{\Gamma L}\Omega}\left(N_\Gamma + \frac{1}{2} \mp \frac{1}{2}\right)\delta\left(E' - E + \Delta E_{L\Gamma} \mp \hbar\omega_{\Gamma L}\right)\delta(p' - p \mp \hbar\beta) \qquad (38)$$

The scattering rate is

$$\frac{1}{\tau(p)} = \frac{\pi D_{\Gamma L}^2 Z_L}{2\rho\omega_{\Gamma L}}\left(N_\Gamma + \frac{1}{2} \mp \frac{1}{2}\right)g\left(E \pm \hbar\omega_{\Gamma L} - \Delta E_{L\Gamma}\right) \qquad (39)$$

where g is the density of states $(g \sim \sqrt{E})$ in the final valley. In GaAs, the intervalley scattering rate rises sharply when the Γ valley electron energy exceeds the minimum energy in the L satellite valley by one intervalley phonon energy. A plot of the function may be found in [2].

4.2.2.4 Carrier-carrier scattering

Carrier-carrier scattering is responsible for the rapid broadening of photoexcited hot carrier distributions. It is important in the redistribution of carriers in energy, but it does not contribute to carrier cooling because it is elastic. Carrier-carrier scattering occurs both as a two body collision and as plasmon scattering which is scattering off a collective mode of the carrier plasma. Plasmon scattering may be an important effect in the experiments described in chapter 6. In that study we examined hot carrier relaxation in the presence of a high density cold background carrier population.

In two body carrier-carrier scattering energy and momentum are conserved:

$$p_1 + p_2 = p_1' + p_2' \tag{40}$$

$$E(p_1) + E(p_2) = E(p_1') + E(p_2') \tag{41}$$

We define a pair transition rate as $S(p_1, p_2 : p_1', p_2')$. This is the probability that carriers with momenta p_1 and p_2 scatter to states with momenta p_1' and p_2'. In the center of mass frame, carrier-carrier scattering has the same form as ionized impurity scattering that we considered earlier so the transition rate is

$$S(p_1, p_2 : p_1', p_2') = \frac{2\pi q^4 / \hbar \kappa_s^2 \varepsilon_0^2 \Omega}{4\left(\frac{p}{\hbar}\right)^2 \sin^2\left(\frac{\alpha}{2}\right) + \frac{1}{L_D^2}} \delta\left(p_1 + p_2 - p_1' - p_2'\right)\delta\left(E(p_1) + E(p_2) - E(p_1') - E(p_2')\right) \tag{4}$$

The scattering rate is evaluated by summing over all final states. In contrast to the other scattering mechanisms that we have considered, however, we now need to take into account the occupancy of the initial and final states. Scattering will only occur when the initial states are occupied and the final states are empty. Therefore the scattering rate is

$$\frac{1}{\tau(p)} = \sum_{p_2}\sum_{p_1} S(p_1, p_2 : p_1', p_2') f(p_2)[1 - f(p_1')][1 - f(p_2')] \qquad (43)$$

where f is the distribution function. The distribution function is calculated by solving the Boltzmann transport equation. This is a difficult task analytically. In our simulations the Boltzmann transport equation is solved by an ensemble Monte Carlo technique which is discussed in section 4.3.

The Pauli principle leads to interesting behavior of the carrier-carrier scattering rate near the Fermi surface. Consider an electron with energy $E_1 > E_F$ scattering with another electron of energy $E_2 < E_F$. After scattering the energies are E_3 and E_4. The Pauli principle limits the possible energies and momenta for E_3 and E_4. If $E_1 = E_F + \delta E$, then E_2 must lie within δE below the Fermi surface, for example. It turns out that the scattering rate is proportional to δE^2 so that carriers right at the Fermi surface have an infinite lifetime.

Plasmon scattering is scattering off of quantized fluctuations in the carrier density which oscillate at the plasma frequency. Analytically, plasmon scattering has the same form as polar optic phonon scattering. Therefore the scattering rate is

$$\frac{1}{\tau(p)} = \frac{q^2 \omega_p}{4\pi \kappa_s \varepsilon_0 \hbar \sqrt{2E(p)/m}} \left(N_p + \frac{1}{2} \mp \frac{1}{2}\right) \ln\left(\frac{\beta_{max}}{\beta_{min}}\right) \qquad (44)$$

The plasma oscillation cannot have a maximum wavevector that corresponds to a wavelength shorter than the screening length, however.

In that case the collision must be treated as a two body process. Therefore the maximum wavevector is either β_{max} or the inverse of the screening length, whichever is shorter. For very high densities, coupled plasmon - LO phonon modes must be considered.

4.2.3 Screening

In our simulations screening is calculated in a "quasidynamic" approximation. The Thomas-Fermi expression is used for Γ valley electrons, light holes, and spin split off holes while screening by heavy holes and satellite valley electrons is neglected. This is justified by the assumption that the high mass of heavy holes and satellite valley electrons prevents them from responding quickly enough to be effective in screening.

The Thomas-Fermi approximation is a static theory of screening; in other words it assumes that screening is instantaneous. In the Thomas-Fermi theory the Coulomb potential is replaced by a Yukawa potential, $\phi(r) = \dfrac{Q}{r}e^{-k_0 r}$ where the screening wavevector is $k_0^2 = 4\pi e^2 \dfrac{\partial n}{\partial \mu}$ [9]. Here, n is the carrier density and μ is the chemical potential.

In our simulation the screening wavevector is given by

$$q_0^2 = \frac{e(p_{lh} + p_{so})}{\varepsilon k_B T_L} + \frac{e n_\Gamma}{\varepsilon \langle E_\Gamma \rangle} \tag{45}$$

where e is the electron charge, the p's are hole densities, T is the lattice temperature, and ε is the static dielectric constant. We use $\dfrac{n}{\langle E \rangle}$ as the simplest possible approximation to $\dfrac{\partial n}{\partial \mu}$. We use kT as the average energy of the holes because the holes are injected at approximately this energy and it's faster than actually calculating the average. The average energy

of the Γ valley electrons is calculated from the time dependent distribution function.

Ideally we would like to use a fully dynamic theory of screening incorporating a frequency and wavevector dependent dielectric function. This would take into account the time it takes carriers to move and participate in screening. Instead we make an assumption that the light effective mass carriers screen instantaneously while the heavy ones don't screen at all. This is what we mean by a "quasidynamic" approximation.

Our screening calculation is also adiabatic in the sense that we assume there is no delay between changes in carrier density and screening wavevector. We update the screening wavevector every 60 fs early in the simulations and less often at later times as the distributions change more slowly. We found by trial and error that if we update the screening wavevector more often than this, the final results don't change.

For the experiments to be described in chapter 5 overall screening is weak. At long times only Γ valley electrons contribute significantly. The light and split off holes become heavy holes quite quickly so they don't make a large contribution to the screening wavevector. At short times the Γ valley electron average energy is high, so they don't screen very much.

4.3 Monte Carlo solution of the Boltzmann tranport equation

The distribution function tells us the probability of finding an electron or hole at a given position, momentum, and time. The equilibrium distribution function is the Fermi-Dirac distribution

$$f(p) = \frac{1}{1 + e^{[E_C(r,p) - E_F]/k_B T_L}} \tag{46}$$

The dynamics of hot electrons in a semiconductor would be completely specified by an accurate knowledge of the distribution function in time starting from photoexcitation and proceeding to the equilibrium Fermi-Dirac function.

4.3.1 The Boltzmann transport equation

The Boltzmann transport equation is a bookkeeping equation that keeps track of changes in the distribution function. The distribution function evolves via carrier generation and recombination and by scattering which moves carriers between different momentum states. The equation is

$$\frac{\partial f}{\partial t} + v \cdot \nabla_r f + F \cdot \nabla_p f = s(r,p,t) + \frac{\partial f}{\partial t}\bigg|_{collisions} \tag{47}$$

where $v = \nabla_p E(p)$, F is the force on carriers (from an electric field, for example), and s is a source term representing generation-recombination processes.

Like many of the equations of physics, the Boltzmann transport equation is easier to state than to solve. One simple method of solution is called the relaxation time approximation for the collision term. In this approximation $\frac{\partial f}{\partial t}\bigg|_{collisions} = \frac{-f_A}{\tau_f}$ where f_A is the momentum antisymmetric part of the distribution function. Under spatially uniform conditions with no applied forces this leads to a solution $f(t) = f_0 + [f(0) - f_0]e^{-t/\tau_f}$. In other words, perturbations die exponentially. Unfortunately, even when an energy dependent relaxation time is used, the relaxation time approximation is only valid for low applied fields and elastic or isotropic scattering, none of which is a good approximation in our case.

The Boltzmann transport equation has some inherent approximations. It is a single particle description of a many particle system and it treats carriers semiclassically as if they obeyed Newton's laws between collisions. Only the scattering events are treated quantum mechanically and even so the Boltzmann equation assumes that collisions take no time and occur at points in space. The distribution function is classical because it assumes that postion and momentum can be known at the same time. It turns out that these limitations do not prevent the Boltzmann equation from representing a valid description of our experiments. With the recent demonstration of sub 10 fs pulsed lasers, however, the validity of the Boltzmann equation may become an issue in the future. At very short times coherent effects between carriers become important.

4.3.2 Monte Carlo methods

The Monte Carlo simulation prcedure has three main steps. Starting from an initial position and momentum each carrier travels for a short time in free flight. At the end of free flight a specific scattering mechanism is selected, and after that the momentum is updated to take the effects of scattering into account.

The first problem is deciding how long the free flight for a given carrier should last. The overall scattering rate is

$$\Gamma(p) = \sum_{i=1}^{k} \frac{1}{\tau_i(p)} \qquad (48)$$

where k is the number of scattering mechanisms included in the model. Γ is a function of energy and time so it is impractical to compute free flight times on the fly. This problem is solved by the method of self scattering. Self scattering is an extra scattering mechanism that is

added to make to total scattering rate constant: $\Gamma_{self}(p) = \Gamma_0 - \Gamma(p)$ where Γ_0 is a constant scattering rate chosen to always be larger than the total real scattering rate. When a particle is selected for self scattering, nothing happens; it just continues in its previous trajectory. Now that the total scattering rate is constant, the probability that a carrier undergoes its first collision between t and t+dt is the scattering rate multiplied by the probability that it hasn't scattered up until t:

$P(t) = \Gamma_0 e^{-\Gamma_0 t} dt$ If the computer generates random numbers, r, evenly distributed between 0 and 1 then it follows that the desired collision times are $t_c = \frac{-1}{\Gamma_0} \ln(r)$. Even though self scattering is the most frequent scattering event, it takes the computer less time to churn through self scatterings than it would to calculate scattering times using the real, energy and time dependent rates [2].

The scattering mechanism is selected using a second random number. The carrier's energy is known just before it scatters so we can construct a graph of the probability of any given scattering event versus energy. We use the lth scattering mechanism when

$$\frac{\sum_{i=1}^{l-1} \frac{1}{\tau_i(p)}}{\Gamma_0} \leq r < \frac{\sum_{i=1}^{l} \frac{1}{\tau_i(p)}}{\Gamma_0} \tag{49}$$

where r is another random number evenly distributed between 0 and 1.

Before the next free flight, both the magnitude and direction of the carrrier's momentum are updated. Since we know the energy, the magnitude of the momentum may be determined from the bandstructure. The polar and azimuthal angles of the new momentum are calculated from two more random numbers, weighted appropriately for the particular type of scattering.

In our simulation, we are concerned with transient phenomena. We use the ensemble method to estimate quantities of interest. For example the average value of an observable A is given by $\langle A(t) \rangle = \frac{1}{N} \sum_i A_i(t)$ where N is the number of particles in the ensemble simulation. There are 40,000 electrons and holes in our model. The code is approximately 10,000 lines long and takes about 10 hours per simulation. The simulation is run on a Cray supercomputer or on a system of about a dozen multiprocessor Sun workstations.

4.3.3 Calculation of the nonlinear absorption and transmission

To compare our simulations to pump-probe experiments we need to calculate the absorption of the pump pulse and the differential transmission of the probe versus pump-probe delay.

We start from no carriers at 200 fs before the pump pulse arrives and introduce electron-hole pairs using the photon energy density

$$N(\hbar\omega,t) = N_0 e^{-4\ln 2(\hbar\omega-\hbar\omega_0)^2/\sigma^2} \text{sech}^2\left(\frac{2t\cosh^{-1}2}{\tau_0}\right) \tag{50}$$

Here ω_0 is the spectral center of the laser pulse and σ and τ_0 are the spectral and temporal full widths at half maximum. By Fermi's Golden Rule the number of optical transitions per unit time per unit volume is

$$W(\omega) = \frac{2\pi}{\hbar}\left(\frac{eA_0}{mc}\right)^2 \sum_{transitions} \int_{BZ} \frac{2d\bar{k}}{(2\pi)^3}\left|H_{\bar{k}\bar{k}'}\right|^2 \delta\left(E_c(\bar{k}) - E_v(\bar{k}) - \hbar\omega\right) \tag{51}$$

where the vector potential is $\bar{A} = \bar{A}_0 e^{i(\bar{k}\cdot\bar{r}-\omega t)}$, and H is the optical matrix element. The absorption, α, is the energy absorbed per unit volume per unit time divided by the energy flux. The energy flux is the energy

density multiplied by the speed of propagation. Symbolically,

$$\alpha(\omega) = \frac{\hbar\omega W(\omega)}{u(c/n)} \text{ where } u = \frac{n^2 A_0^2 \omega^2}{2\pi c^2}.$$

Therefore we may write the absorption as

$$\alpha(t) \propto \frac{1}{\omega}\int d\hbar\omega \int dt' \, N(\hbar\omega, t-t')\sum_v \int d\bar{k} \left|H_{\bar{k}\bar{k}'}\right|^2 \delta[E_c(k) - E_v(k) - \hbar\omega][1 - f_c^e(\bar{k}, t') - f_v^h(\bar{k}, t')] \quad (52)$$

where we have set constant factors in front of the integral equal to one.
The factor $1 - f_e - f_h$ comes from considering the probability of absorbing
a photon minus the probability of emitting a photon by stimulated
emission: $(1 - f_e)(1 - f_h) - f_e f_h = 1 - f_e - f_h$. It is important to emphasize that
differential transmission measurements are sensitive to the sum of the
electron and hole distribution functions. Luminescence, on the other
hand, is sensitive to the product $f_e f_h$. The two techniques reveal
complementary information.

The change in absorption is

$$\Delta\alpha(t) \propto \frac{-1}{\omega}\int d\hbar\omega \int dt' \, N(\hbar\omega, t-t')\sum_v |H_v(\hbar\omega)|^2 [f_c^e(\hbar\omega, t') + f_v^h(\hbar\omega, t')] \quad (53)$$

In these expressions N is the transient photon energy density and
$f(\hbar\omega, t)$ is the time dependent distribution function in the optically
connected region. In the case of isotropic bands f is equal to the regular
distribution function which is a function of energy. The differential
transmission is derived from the differential absorption:

$$\frac{\Delta T(t)}{T_0} \propto \frac{1}{\omega}\int d\hbar\omega \int dt' \, N(\hbar\omega, t-t')\sum_v |H_v(\hbar\omega)|^2 [n_c^e(\hbar\omega, t') + n_v^h(\hbar\omega, t')] \quad (54)$$

In the thin sample limit, the connection between $\Delta T/T$ and $\Delta\alpha$
comes about in the following way. The intensity transmitted through the
sample is, $I_{transmitted} = I_{incident}e^{-\alpha x}$, where α is the absorption and x is the
sample thickness. We measure $\frac{\Delta T}{T} = \frac{I_{pump\_on} - I_{pump\_off}}{I_{pump\_off}}$. If α_0 is the
absorption with the pump off and α is the absorption with the pump on

63

then, $\dfrac{\Delta T}{T} = \dfrac{I_{incident}\left(e^{-\alpha x} - e^{-\alpha_0 x}\right)}{I_{incident}e^{-\alpha_0 x}} \cong \Delta \alpha x$ where $\Delta \alpha = \alpha - \alpha_0$. The approximate

equality holds when $\Delta \alpha x$ is small. Our samples are less than one

absorption depth thick and we measure peak changes in transmission on

the order of 10^{-2} so the thin sample limit is a good approximation for our

experiments.

4.4 Conclusion

In this chapter we briefly pointed out some of the essential features

of the procedure that we use to simulate our experimental results. We

showed how the method makes the connection all the way from the

fundamental physics of carrier scattering to the prediction of the

observed pump-probe differential transmission.

We use a k•p method to calculate an accurate bandstructure and

scattering rates. An ensemble Monte Carlo simulation incorporating

40,000 electrons and holes is used to solve the Boltzmann transport

equation. This gives us the time dependent carrier distribution functions

which is the desired physical description of hot carrier dynamics. Finally

we compute the nonlinear differential absorption in order to compare the

predictions of the simulation to experiment.

4.5 References

[1]   C. Jacoboni and L. Reggiani, "The Monte Carlo method for the

solution of charge transport in semiconductors with applications to

covalent materials." Reviews of Modern Physics, **55**, p. 645-705 (1983).

[2]   M. Lundstrom, <u>Fundamentals of Carrier Transport</u>, Volume X of <u>Modular Series on Solid State Devices</u>, edited by G. W. Neudeck and R. F. Pierret, Addison-Wesley, New York, 1990.

[3]   B. K. Ridley, <u>Quantum Processes in Semiconductors</u>, Clarendon Press, Oxford, 1982.

[4]   F. H. Pollak, C. W. Higginbotham, and M. Cardona, "Band structure of GaAs, GaP, InP, and AlSb: The k•p method," Journal of the Physical Society of Japan, **21** supplement, p. 20-26 (1966).

[5]   M. Cardona and F. H. Pollak, "Energy band structure of germanium and silicon: The k•p method," Physical Review, **142**, p. 530-543 (1966).

[6]   D. W. Bailey, C. J. Stanton, and K. Hess, "Numerical studies of femtosecond carrier dynamics in GaAs," Physical Review B, **42**, p. 3423 (1990).

[7]   G. D. Sanders, private communication.

[8]   J. D. Wiley, "Polar mobility of holes in III-V compounds," Physical Review B **4**, p. 2485 (1971).

[9]   N. W. Ashcroft and N. D. Mermin, <u>Solid State Physics</u>, Saunders College, Philadelphia, 1976, p. 342.

Chapter 5
Tunable Femtosecond Spectroscopy in $Al_{0.1}Ga_{0.9}As$

5.0 Introduction

In this chapter we present an investigation of the femtosecond dynamics of photoexcited carriers in $Al_{0.1}Ga_{0.9}As$ [1]. Tunable femtosecond absorption saturation measurements are compared with ensemble Monte Carlo simulations to determine the time evolution of the nonequilibrium carrier distributions.

The experiments are performed with an amplified femtosecond laser system. Continuum generation and Fourier synthesis are used to create a tunable source of 40 fs optical pulses. These pulses excite carriers to initial distributions at various energies in the conduction band depending on the wavelength chosen. After initial excitation the distributions are probed by pulses at the same wavelength as the pump, delayed in time. We vary the energy of the initial carrier distributions to position them near in energy in the conduction band to the threshold for scattering to the L satellite valley.

We interpret the results by comparison to theoretically predicted absorption saturation data which is based on Monte Carlo simulations of the hot carrier dynamics.

5.1 Experiments

We have performed a series of pump-probe absorption saturation experiments using a laser system based on an amplified CPM ring dye laser [Figure 5.1].

Fig. 5.1 Tunable pump-probe experiment
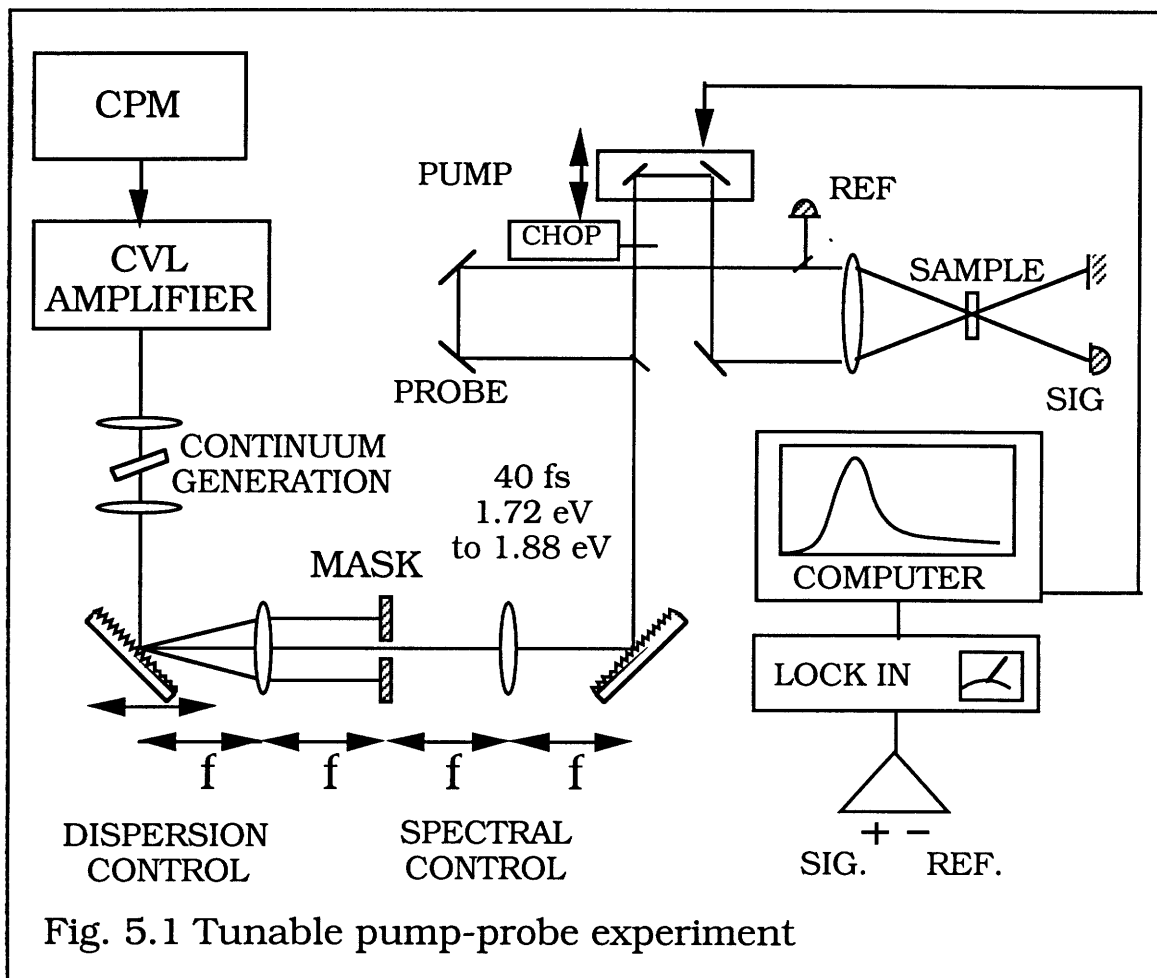
Femtosecond laser pulses from the CPM are amplified in a copper vapor laser pumped dye amplifier. The amplified pulses are focussed into a flowing jet of ethylene glycol to generate a femtosecond white light continuum, a portion of which is spectrally filtered in a grating Fourier synthesizer. Finally the pulses are directed to a pump-probe set up where the differential transmission is measured.

The CPM laser, the copper vapor laser pumped dye amplifier, and continuum generation have been described in chapter 3. The continuum

is intense enough to provide pump pulses for experiments anywhere in the range from 500 to 800 nm without further amplification. We use a grating Fourier filter [2] to select the desired spectrum from the continuum. The filter consists of two gratings separated by a unity magnification telescope. The spacing of the gratings and lenses determines the chromatic dispersion of the device. In fact the system is optically equivalent to the standard arrangement that provides negative group velocity dispersion [3] except that the lenses permit a positive or negative effective distance between the gratings. The spectrum of the continuum in imaged in the Fourier plane and a variable width slit is used to select the center wavelength and bandwidth of the pulses to be sent to the experiment. More sophisticated masking techniques [4] may be used to create exotic pulse shapes or pulse trains in the time domain. Our apparatus eliminates the need for an interference filter to select the wavelength. This is important because interference filters' typical maximum transmission is only 50 %. Because the Fourier filter compensates for dispersion in the rest of the optical system and balances self phase modulation from continuum generation, the output pulses are as short as 40 fs.

The tunable pulses are sent to a pump-probe optical set up. A portion of the probe beam is split off as a reference and detected by a high sensitivity photodiode. The pump beam is polarized perpendicular to the probe with a zero order half wave plate and modulated with a chopper wheel. The transmitted probe is detected by a second high sensitivity photodiode matched to the reference detector. The reference level is subtracted from the probe signal in a low noise preamplifier (Stanford Research 565) the output of which is fed to a lockin amplifier

(Princeton Applied Research 128A). The delay between the pump and probe pulses is varied by mounting two mirrors in the pump arm on a computer controlled mechanical stage (Klinger UT100PP) that moves in 0.1 μm steps. Each step changes the delay between the pump and probe by 0.66 fs.

We take data by scanning the pump-probe delay and recording the signal detected by the lockin with an analog to digital converter. The smallest change in transmission that we can detect is approximately 10^{-4}. The limiting factors in our detection sensitivity are the nonlinear amplification of noise inherent in continuum generation and copper vapor laser instabilities. Our signal to noise ratio allows us to resolve the dynamics of photoexcited carrier densities as small as 5×10^{17} cm^{-3}.

The measurements are performed at room temperature on 0.2 μm thick samples grown by molecular beam epitaxy by Dr. C. Wang at MIT Lincoln Laboratory [Figure 5.2].

Fig. 5.2 AlGaAs MBE samples

In the figure:
- AR Coating
- Cladding Layer: $Al_{0.6}Ga_{0.4}As$ — 0.5 μm
- Sample: $Al_xGa_{1-x}As$ — 0.2 μm
- Cladding Layer: $Al_{0.6}Ga_{0.4}As$ — 0.5 μm
- Quartz Substrate
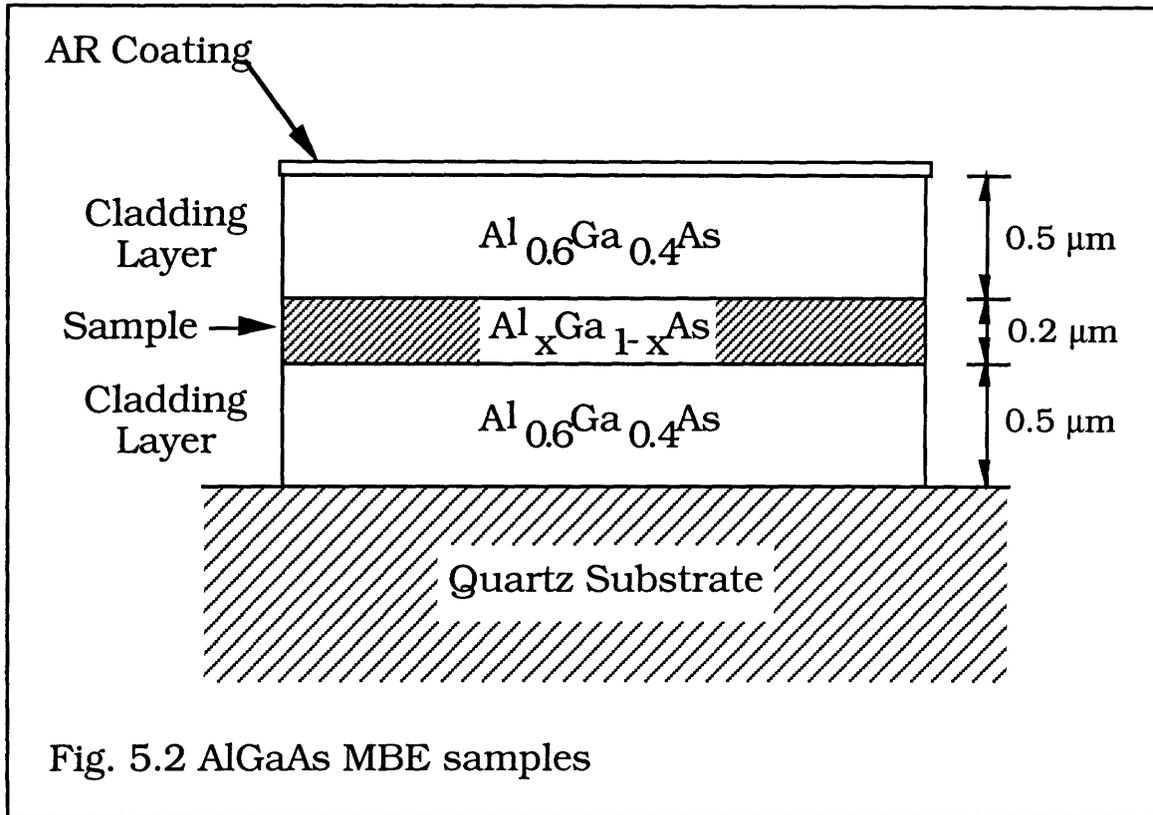
The 0.2 um layer is sandwiched between 0.5 um layers of $Al_{0.6}Ga_{0.4}As$. The samples are mounted on a quartz substrate with optical cement. The side that is not glued to the quartz is antireflection coated. Our samples are thinner than those used in previous studies. The sample thickness in our case is less than one optical absorption depth so the density of excited carriers is uniform along the beam propagation direction and carrier diffusion effects [5] are minimized.

The mole fraction of aluminum is chosen at 0.1 for the purpose of isolating the effect of intervalley scattering in carrier relaxation (see Fig. 4.2). As the pump photon energy is increased from 1.72 eV the initial photoexcited electron distribution moves to higher and higher energies in the Γ valley of the conduction band. By approxomately 1.82 eV the photoexcited electrons are energetic enough that deformation potential scattering to the L satellite valley is possible. At about 1.88 eV the

transition from the spin split off band to the bottom of the Γ valley becomes energetically allowed, complicating the absorption saturation dynamics. The small energy window from 1.82 eV to 1.88 eV allows us to isolate the effect of intervalley scattering on the hot electron dynamics.

5.2 Results and discussion

We will discuss the results of this study in four parts: the optically coupled region, simulated time dependent hot carrier distributions, measured and simulated differential absorption data, and the effect of varying various parameters in the Monte Carlo simulation. This discussion reflects both the flow of predictions in the theory and the propagation of experimental results back to fundamental measurements. While the experimental results could be used alone to determine relaxation time constants for the absorption saturation, Monte Carlo simulation has allowed us to go one step farther and extract the hot carrier dynamics that cause the optical response.

5.2.1 Optically coupled region

In Figure 5.3 [a,b,c] we show a detailed view of the bandstructure of $Al_{0.1}Ga_{0.9}As$ near the center of the Brillouin zone.

71
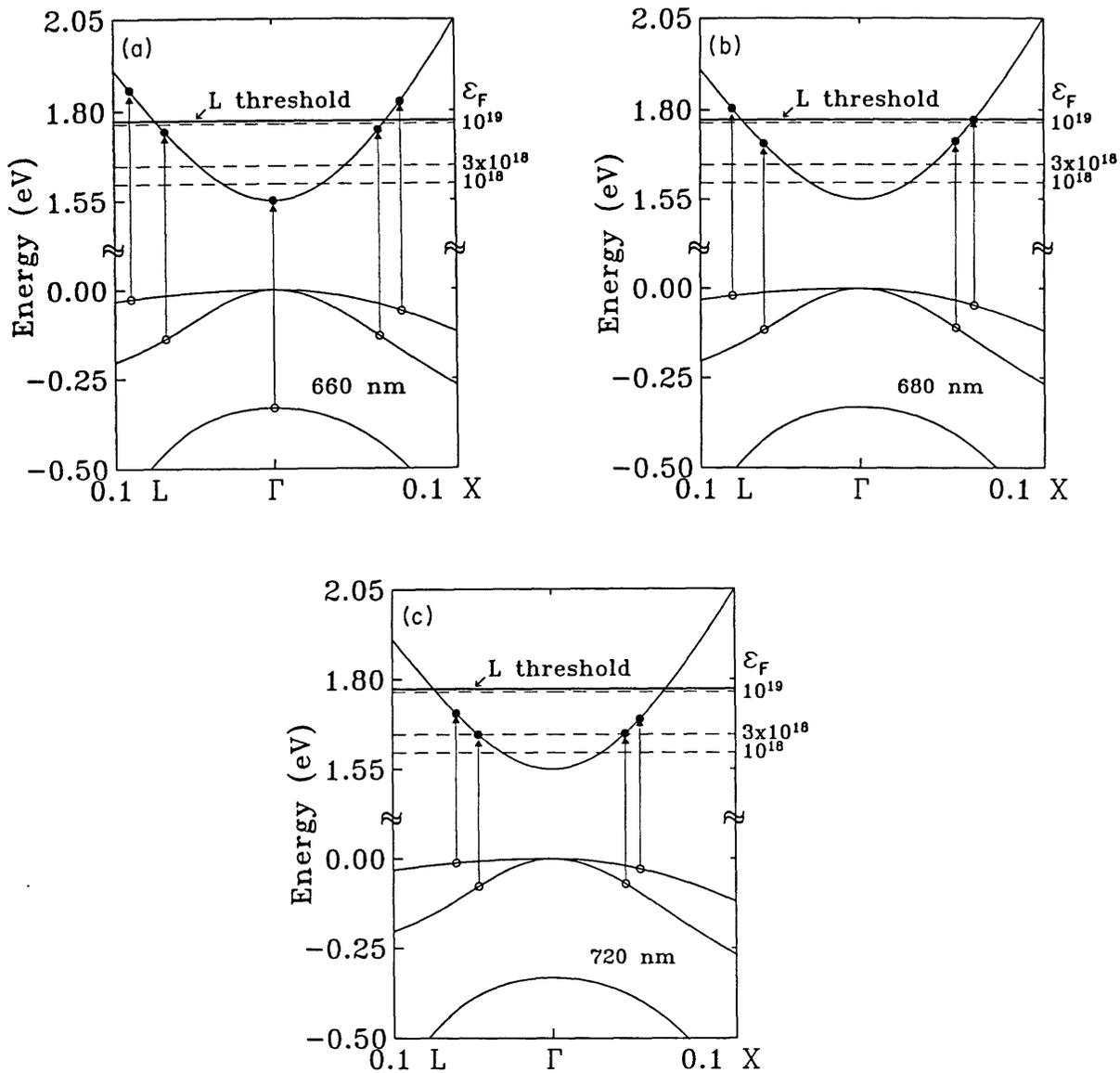
Fig. 5.3 Bandstructure of $Al_{0.1}Ga_{0.9}As$ near the center of the Brillouin zone.

The allowed optical transitions are shown for three different photon energies: 1.88 eV (660 nm), 1.82 eV (680 nm), and 1.72 eV (720 nm). The vertical arrows indicate transitions from the heavy hole, light hole, and spin split off hole valence bands to the Γ valley of the conduction band. The solid horizontal line is drawn at the minimum energy in the L satellite valley. Carriers photoexcited to regions of the Γ valley higher in energy than this line (by at least one phonon energy) can scatter to L.

The dashed horizontal lines indicate the quasi Fermi level for three different photoexcited carrier levels: 10^{18} cm^{-3}, 3 x 10^{18} cm^{-3}, and 10^{19} cm^{-3}.

At 660 nm transitions are possible from all three hole bands and carriers originating from the heavy hole band are placed well above the threshold for intervalley scattering to L. The electrons that come from the light hole band end up just below the L threshold, while those from the spin split off band are excited very close to the band gap. The spin split off transition is not allowed at 680 nm and the electrons excited from the light hole and heavy hole bands are placed at lower energies compared to the 660 nm case. Intervalley scattering is still possible for a fraction of the photoexcited carriers. At 720 nm photoexcited carriers do not undergo intervalley scattering. The transition is low enough in the band that we may expect to see density effects in the pump-probe data, however.

5.2.2 Simulated, time dependent hot carrier distributions

The time evolution of the carrier distribution functions is the most important physical information that we have extracted from our experimental results using Monte Carlo simulation. In Figure 5.4 we show the distribution of electrons in the Γ valley at the temporal center of a 40 fs laser pulse for three different wavelengths.
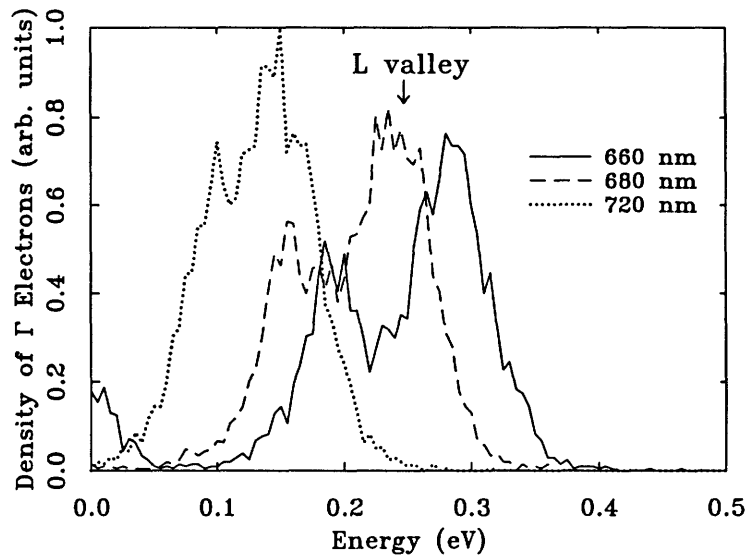
Fig. 5.4 Initial distribution of electrons in the Γ valley.

Energy is plotted horizontally and 0.0 eV corresponds to the conduction band edge. The curves are normalized so that the number of electrons represented by each one is the same. The double (triple for 660 nm) peaked shape reflects the heavy hole and light hole transitions. The width of the peaks is due to three factors: the spectral width of the femtosecond laser pulse, the different dispersion of the band structure in the L and X directions, and the broadening effect of carrier-carrier scattering.

The position of the minimum energy in the L valley is indicated in the figure by the arrow. For the 660 nm transition, more than half the photoexcited carriers lie above this energy while only about one quarter do so for the 680 nm case. Intervalley scattering is negligible at 720 nm.

The time evolution of the Γ valley electron distribution and the three hole band distributions is shown in Figures 5.5 [a,b,c,d], 5.6 [a,b,c,d], and 5.7 [a,b,c]. We examine the distributions' relaxation

dynamics for 660, 680, and 720 nm at 0, 100, and 500 femtoseconds after the center of the excitation pulse.
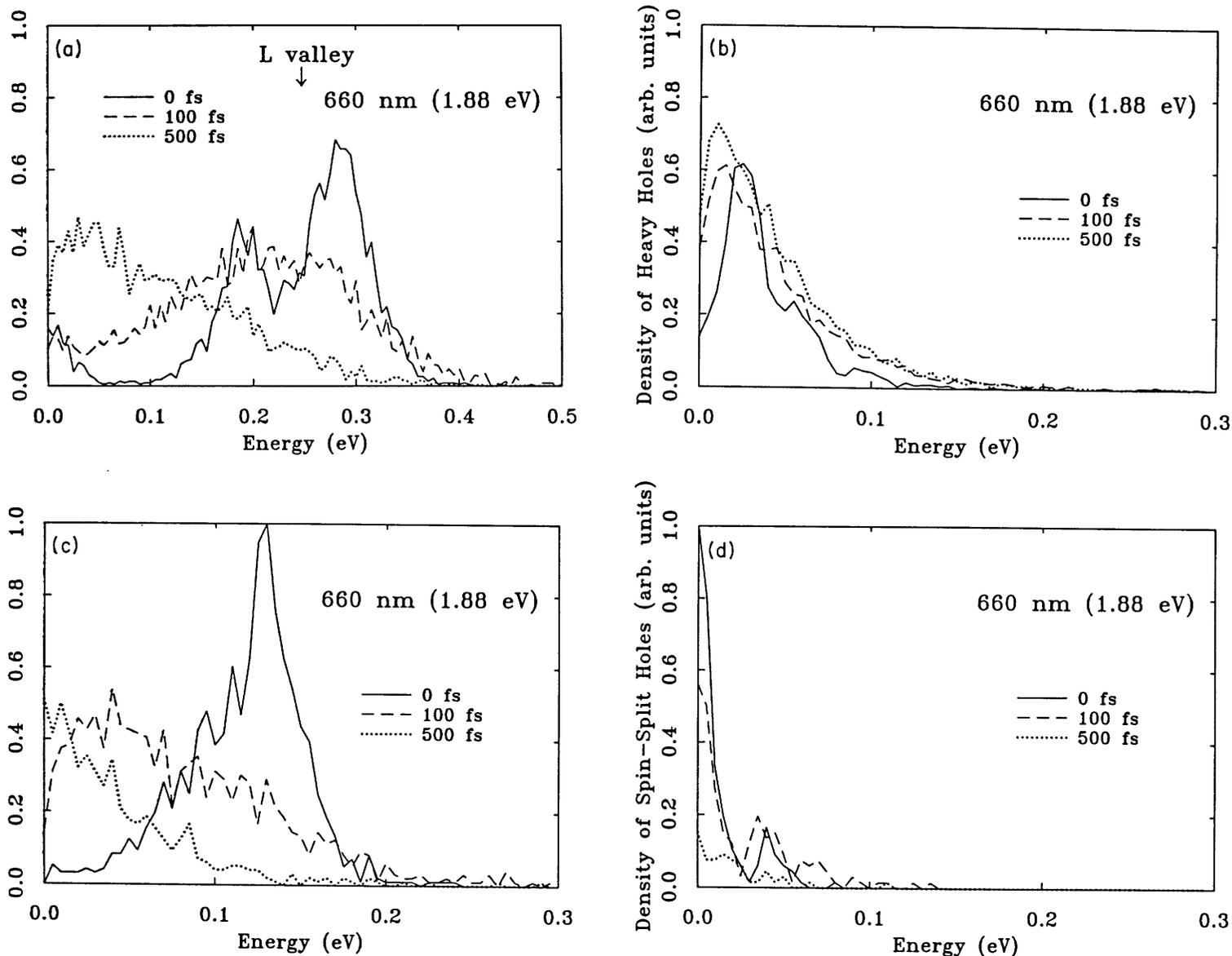
Fig. 5.5 Simulated carrier distributions for 660 nm photoexcitation.
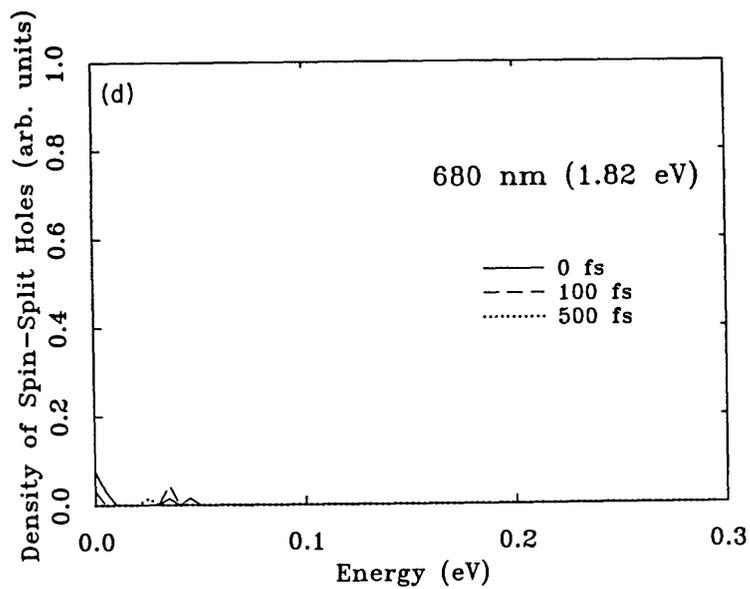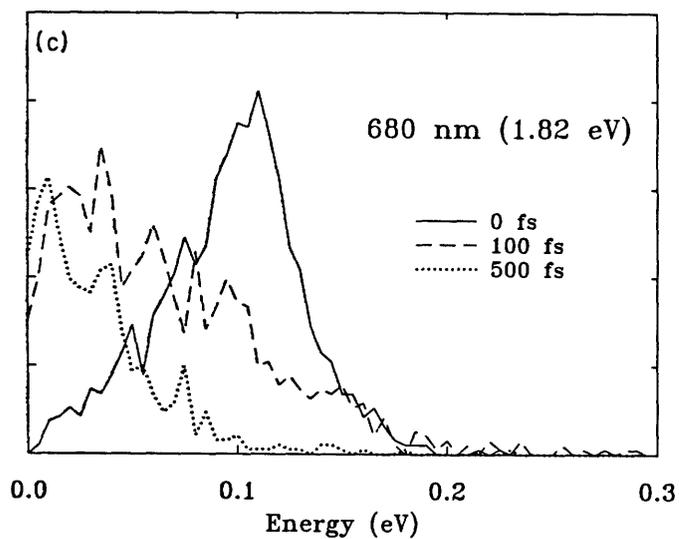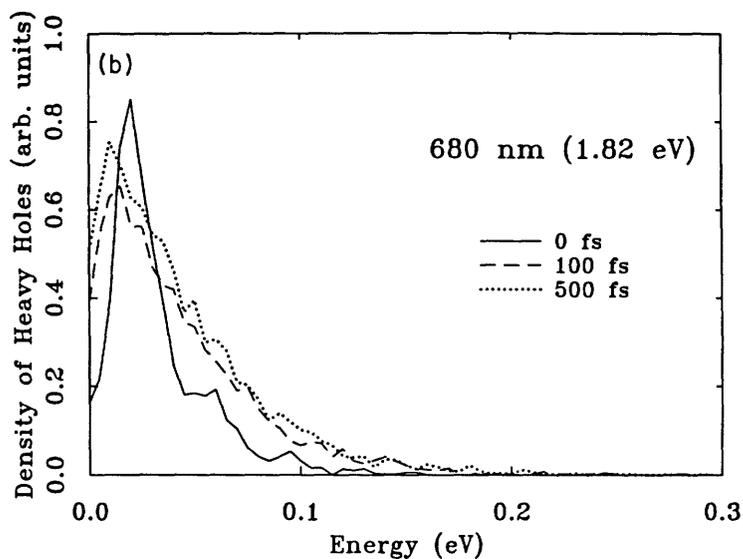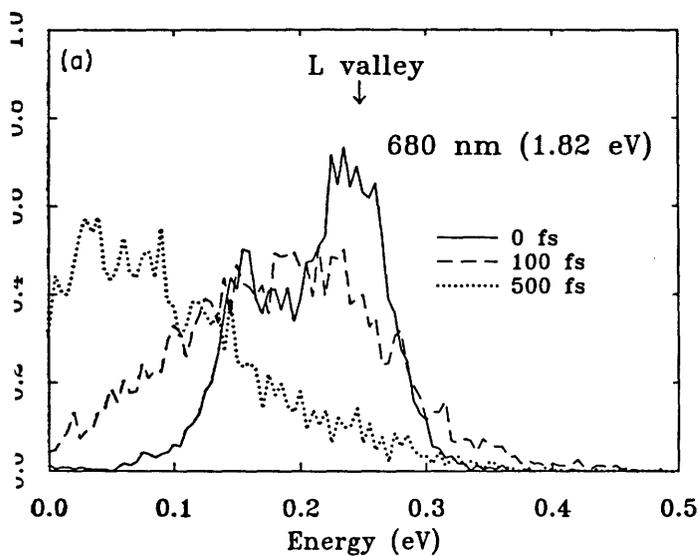
Fig. 5.6 Simulated carrier distributions for 680 nm photoexcitation.
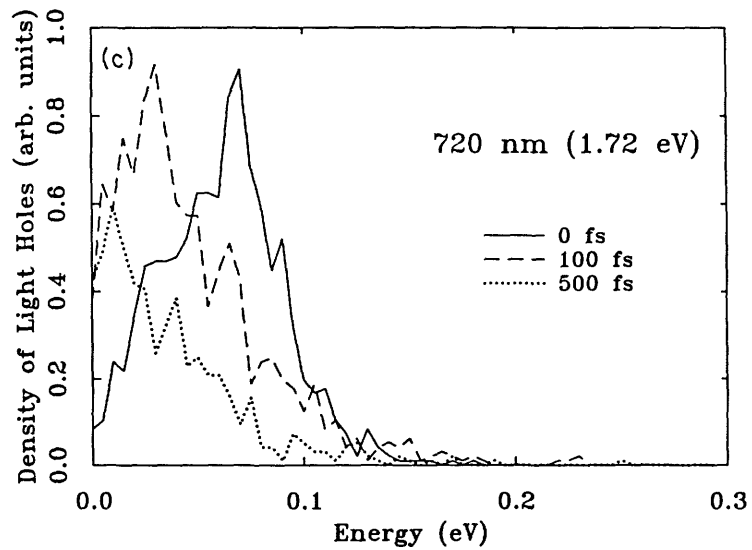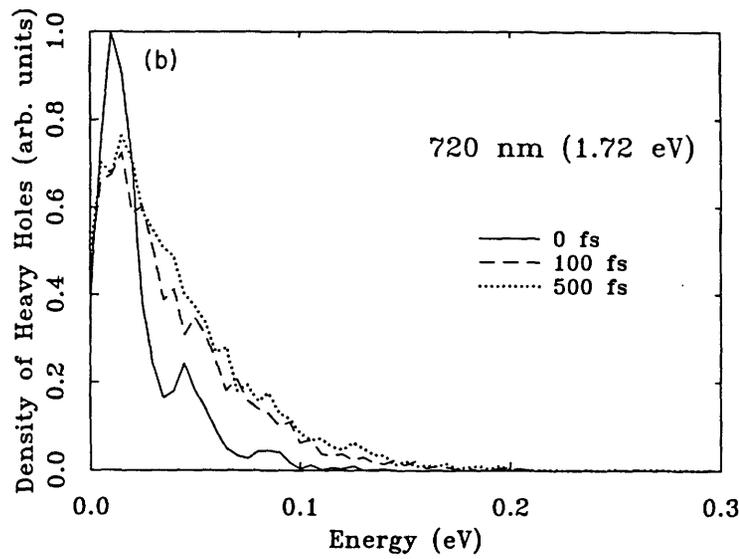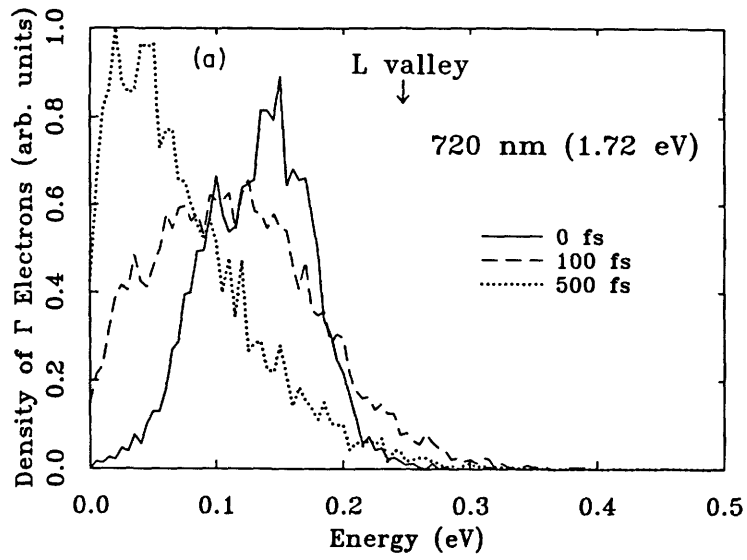
Fig. 5.7 Simulated carrier distributions for 720 nm photoexcitation.

In the first 100 fs after photoexcitation the most important relaxation mechanisms for electrons are carrier-carrier scattering and intervalley deformation potential scattering. At 100 fs the Γ valley electron distribution has broadened significantly at all three wavelengths. The peaks reflecting the individual transitions have disappeared. At 660 and 680 nm many of the electrons scatter to the L satellite valley. In the first 500 fs the electrons lose energy by polar optic phonon scattering and as a result the distribution shifts to lower energies as shown by the trace for 500 fs.

The heavy holes are excited in a relatively narrow band of energies even for a wide distribution of wavevector because of their high effective mass. Therefore the heavy hole relaxation in energy is not as dramatic as that of the electrons.

The light holes are initially excited in a broad peak which indicates the energy of the transition to the Γ valley. The width of the peak comes from the spectral width of the laser pulse and from the shape of the light hole band. There is a larger difference in the light hole dispersion than in the electron dispersion looking in the L and X directions. The light holes scatter rapidly and their energy distribution has not only spread out but also cooled significantly by 100 fs.

The spin split off holes have a significant population at 660 nm, a very small number excited at 680 nm, and none excited at 720 nm. The spin split off hole distribution is always peaked near the band edge. In the 660 nm case we can observe two interesting phenomena. First, the peak amplitude decays as the spin split off holes become light and heavy holes. Second there are small peaks at higher energies than the main

peak. These are the remnants of optical phonon scattering. The carrier density is low for the split off holes so carrier-carrier scattering is weak within the band. Thus phonon peaks are not dissipated as rapidly as for the electrons or heavy and light holes.

5.2.3 Measured and simulated differential transmission

The time dependent carrier distribution functions are the central theoretical result from this study. They are not directly observable in our experiment, however. We have measured the change in transmission of a weak optical probe pulse as a function of time delay between the pump and probe pulses. In order to compare our experiment to theory we calculate predicted differential transmission versus pump-probe delay using our calculated time dependent distribution functions.

In Figures 5.8, 5.9, 5.10, 5.11, and 5.12 we show experimentally measured and theoretically calculated $\Delta T/T$ versus pump-probe delay for five different laser wavelengths: 660, 670, 680, 690, and 720 nm which correspond to 1.88, 1.85, 1.82, 1.80, and 1.72 eV respectively. Probe delay is scanned from -250 fs to +1000 fs after the pump. The experimental data represent averages over 10-20 scans. At each wavelength we show data at two different densities. We can determine relative densities within a single wavelength data set to good accuracy, but the error in the absolute estimate of carrier density may be as much as a factor of 5. This is mainly due to difficulty in determining the optical spot size on the sample.

The Monte Carlo technique allows us to determine the physical processes that are responsible for the dynamics of the differential transmission. It should be emphasized that the overall comparison

displayed in the series of figures is the output of simulations that differ only in the experimentally varied parameters wavelength and density. There is no fitting of individual curves. Thus the simulation is accurate over a broad range of energies and may be expected to predict phenomena at other energies.
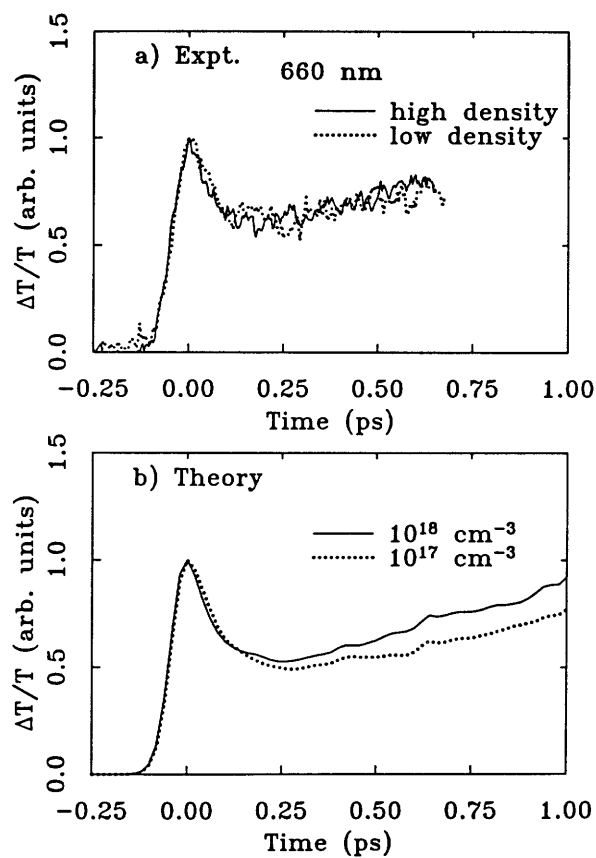
Fig. 5.8 Differential transmission versus probe delay at 660 nm.
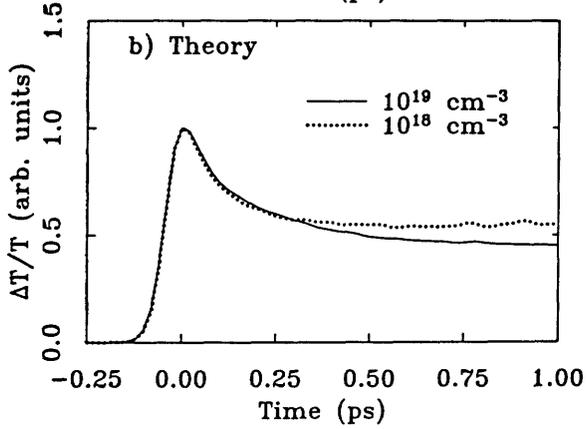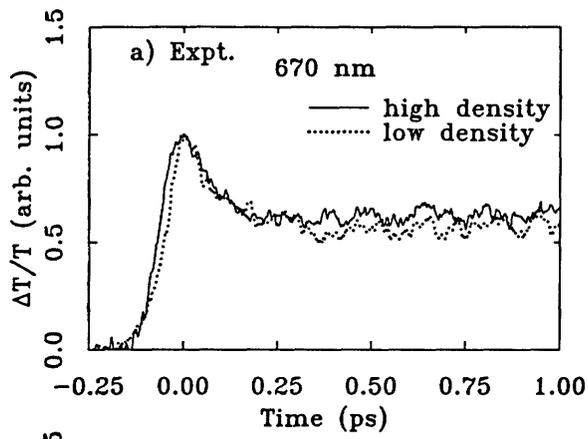
Fig. 5.9 Differential transmission versus probe delay at 670 nm.
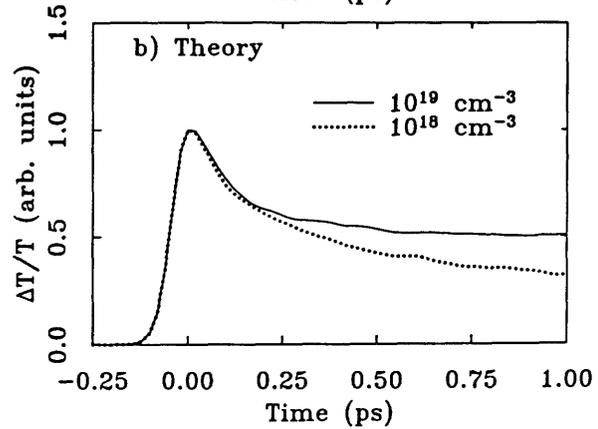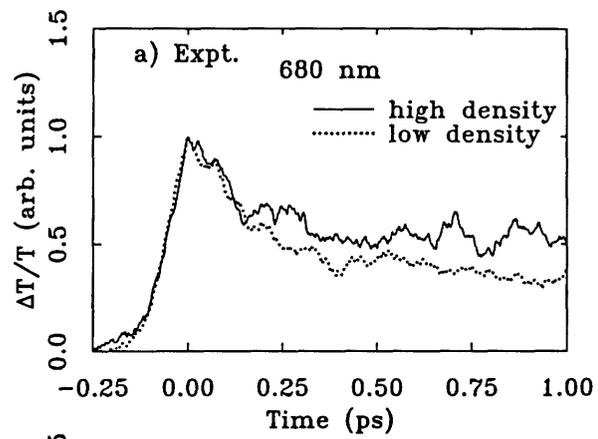

Fig. 5.10 Differential transmission versus probe delay at 680 nm.
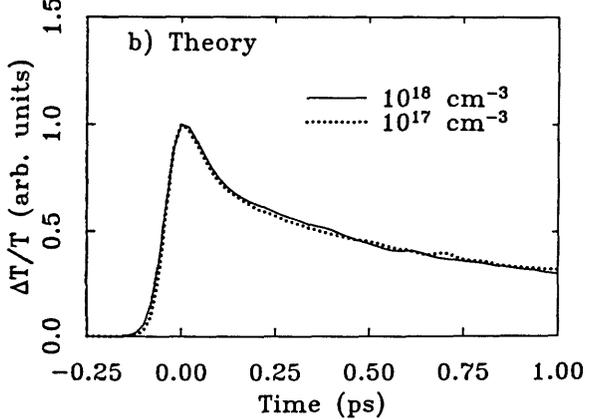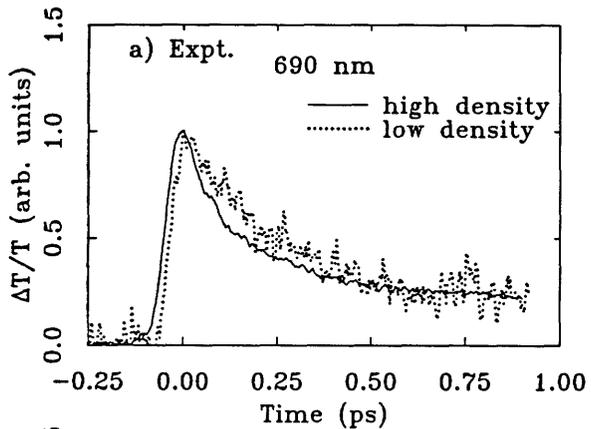
Fig. 5.11 Differential transmission versus probe delay at 690 nm.
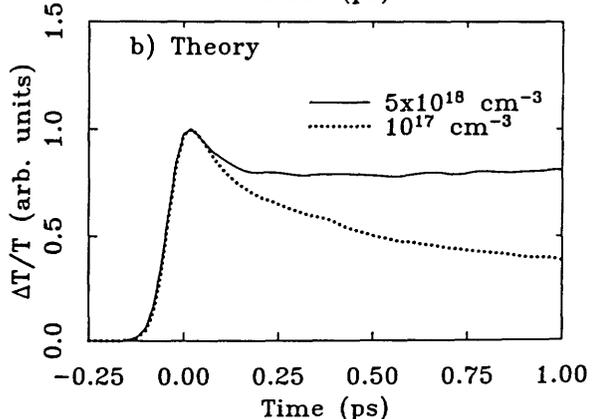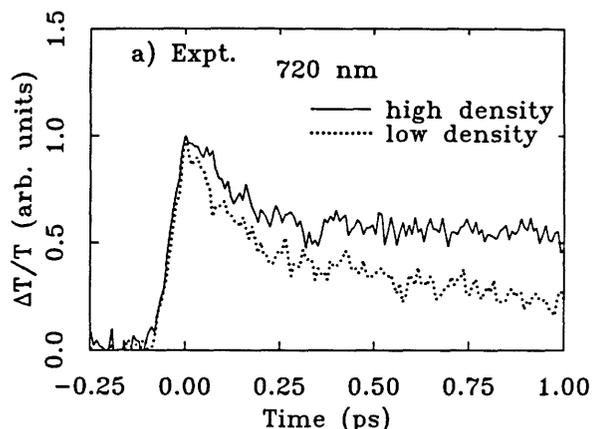

Fig. 5.12 Differential transmission versus probe delay at 720 nm.

The basic structure of the differential transmission curves is the same in all cases. The transmission increases rapidly at zero delay and a short spectral hole burning peak is clearly evident. The transient tail at positive delays reflects changes in the occupancy of states that are measured by the probe pulse. The details of the curves at each wavelength underlie a more precise interpretation of the data.

At 660 nm the hole burning peak is less than 100 fs wide. This short time indicates fast scattering of carriers out of their initial states. The peak is faster at 660 nm than at longer wavelengths because of the effect of scattering to the L valley. The 660 nm trace is also remarkable because the differential transmission increases after 250 fs probe delay. The rise reflects the probe's sensitivity to carriers at the bottom of the conduction band which are probed by transitions from the spin split off band. As carriers return from L and relax to the band edge, states near the bottom of the band fill up. The rising wing in the data is the signature of this effect. This effect becomes weaker at 670 nm and 680 nm and disappears at 690 nm.

As the wavelength is increased and the photon energy is decreased, the hole burning peak becomes broader. Fewer electrons undergo intervalley scattering in the 670 nm and 680 nm cases compared to 660 nm, for example. Since electrons remain in their initial states longer when intervalley scattering is absent, the transient peaks in the data become longer.

When the pump and probe are set to 720 nm, the photoexcited electron distribution is peaked about 150 meV above the band edge. This is close enough to the band edge that we are able to observe the effect of the Fermi level rising with injected carrier density. At long probe

82

delays the differential transmission remains at a higher level as the carrier density in the conduction band increases.

The calculated differential transmission is shown in the lower half of each figure. The calculations fit the experimental data quite well. Both the short and long time behavior are accurately predicted as a function of wavelength as is the density dependence. We conclude that the calculated carrier distribution functions shown earlier must be accurate.

5.2.4 Variation of Monte Carlo parameters

Since we have focussed on the role of intervalley scattering we have varied the deformation potential constant, $D_{\Gamma-L}$, in the simulation to see how sensitive our experiment is to this parameter. These results are shown in Figures 5.13, 5.14, and 5.15.
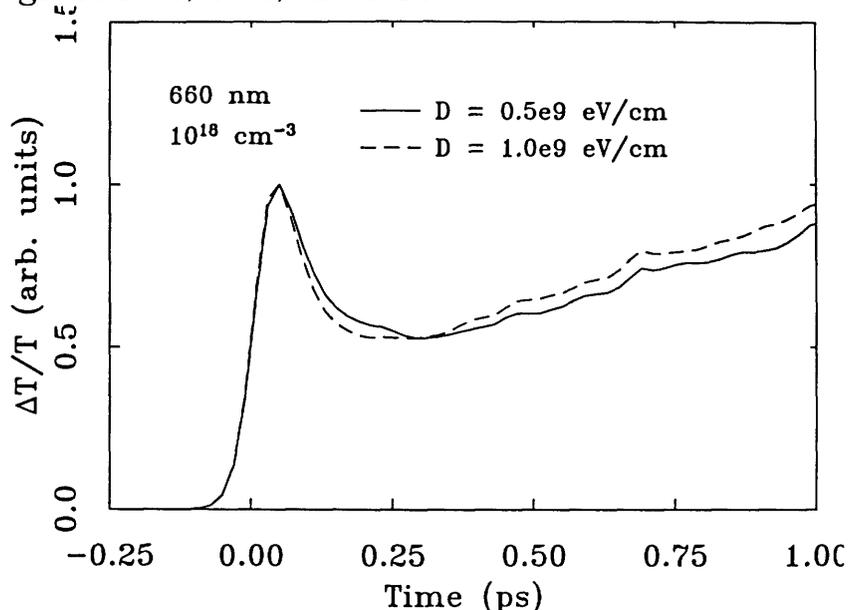

Fig. 5.13 Differential transmission at 660 nm for two different values of $D_{\Gamma L}$.

In Figure 5.13 we show the differential transmission at 660 nm calculated from simulations in which the deformation potential constant

was $0.5\times10^9 eV/cm$ and $1.0\times10^9 eV/cm$. The differential transmission

behavior is not particularly sensitive to changes in the deformation

potential constant. At 660 nm only about one third of the photoexcited

carriers scatter to the L valley. It would be desirable to decrease the

laser wavelength even more so that most of the carriers would be affected

by intervalley transfer, but at wavelengths shorter than 660 nm the

transition from the split off band to the bottom of the conduction band

dominates the pump-probe signal. However our data are consistent with

$D_{\Gamma L} = 5\times10^8 eV/cm$ which is similar to previously reported values.

In Figures 5.14 and 5.15 we show the individual contributions to

the differential transmission at 660 nm from the various electron and

hole distributions for two different values of the deformation potential

constant.
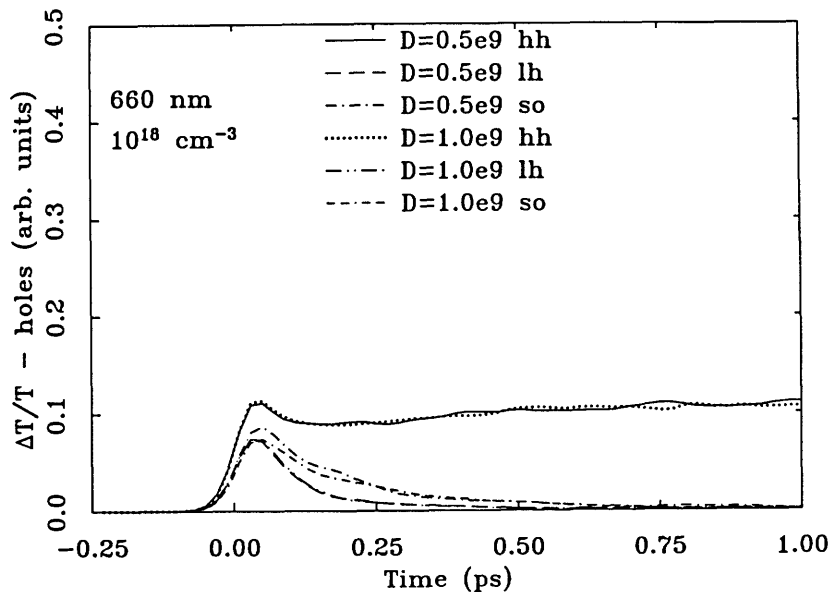
Fig. 5.14 Differential transmission at 660 nm due to
holes for two different values of $D_{\Gamma L}$.
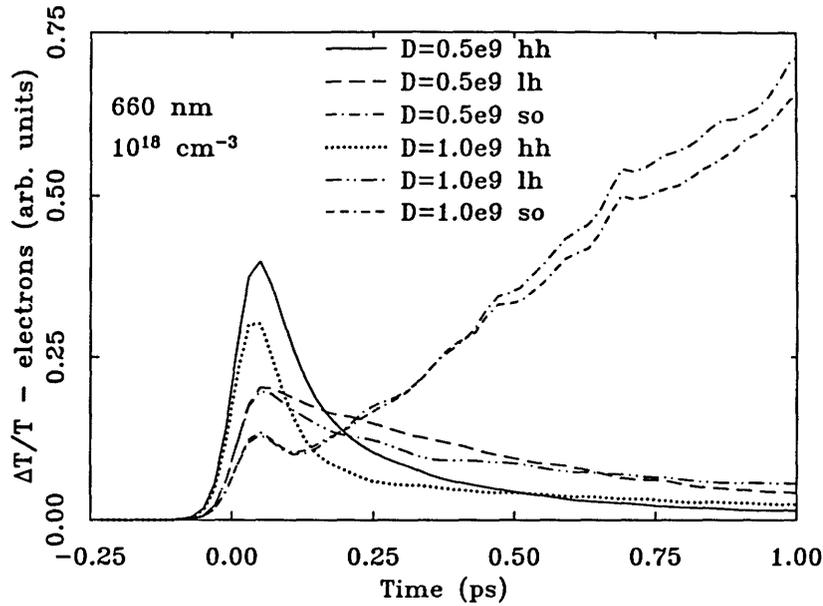
Fig. 5.15 Differential transmission at 660 nm due to electrons for two different values of $D_{\Gamma L}$.

Figure 5.14 shows contributions from holes in the valence band while Figure 5.15 shows contributions from electrons in the conduction band. In Figure 5.15 the electrons are separated according to which valence band they were excited from: heavy, light, or split off hole. For the holes there is little difference between the two values of $D_{\Gamma-L}$. In the case of the electrons, the largest change in signal from varying $D_{\Gamma-L}$ appears in the response due to heavy holes. This makes sense since it is those electrons that are excited high enough in the conduction band to be affected by intervalley scattering as shown in Figure 5.3a.

Overall the experiment is not as sensitive to $D_{\Gamma-L}$ as we would like. In Fig. 5.13 we do note that the initial transient is faster for larger values of $D_{\Gamma-L}$ than for smaller values. When intervalley scattering is stronger carriers leave their initial states more quickly. They also return from L quicker which can be seen as an enhanced rise at long times. The ratio of the Γ to L scattering rate to the return rate, L to Γ, is essentially the ratio of the densities of states in the two valleys. One factor leading to

the lack of sensitivity is that carriers scatter to energies near the bottom of the L valley where the density of states is low compared to higher energies in L.

Finally we considered the effect of varying the optical bandwidth of the laser pulse. This parameter is relatively well known experimentally, but it has a significant effect on the data. In Figure 5.16 we show calculated 720 nm data assuming two different laser bandwidths at two different carrier densities.
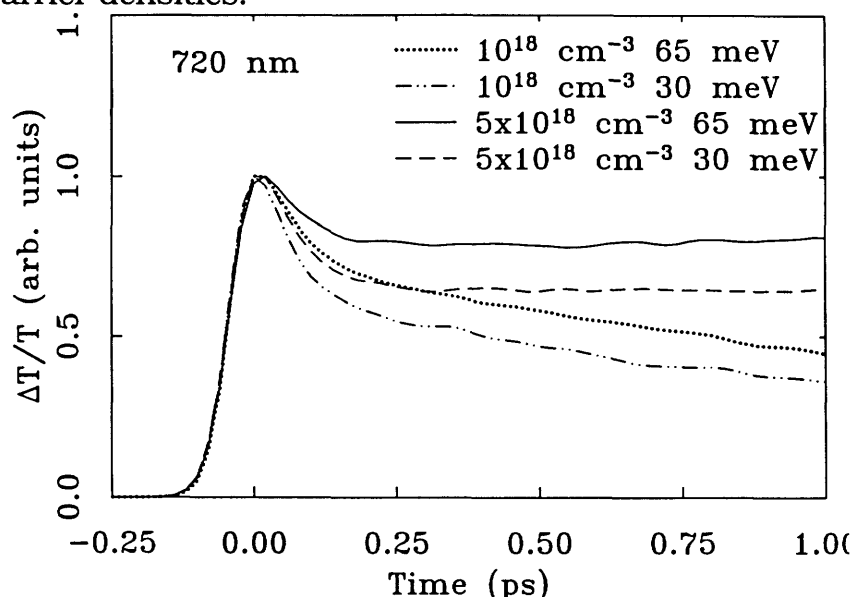

Fig. 5.16 Differential transmission at 720 nm for two different values of laser pulse bandwidth and photoexcited carrrier density.

The 30 meV bandwidth is close to transform limited while the 65 meV width is about 2 times the transform limit for 40 fs pulses. The results show that small errors in the bandwith lead to different pump-probe data. From a theoretical point of view the bandwidth is important because the effective energy spread of photoexcited carriers depends on dephasing as well as the spectrum of the pulse. Carriers are injected in the simulation with a pulse that has independently adjustable duration and bandwidth.

We see that the effect of varying the bandwidth of the laser pulse is larger than that of changing the deformation potential constant for some choices of parameters. In fact, the laser bandwidth is known to within 5 meV. Collisional broadening may change the effective bandwidth, however. We could see a larger effect in the variation of the deformation potential constant, but $D_{\Gamma-L}$ is already known to within an order of magnitude from other experiments.

5.3 Conclusions

We performed an investigation of femtosecond carrier dynamics in $Al_{0.1}Ga_{0.9}As$ using tunable femtosecond pump-probe spectroscopy. Previous work in GaAs had concentrated on dynamics near the band edge or far above the band edge. We have demonstrated that our tunable femtosecond laser system enables us to look at a wide range of photoexcitation enegies. The tunablility permits us to selectively turn on and off various scattering mechanisms to extract more detailed information on the carrier dynamics than was previously possible. We have filled in the gap between previous 2 eV and band edge studies.

We used Monte Carlo simulations to model the carrier dynamics. The Monte Carlo method is the only way that the time dependent carrier distribution functions can be extracted from pump-probe data. Because of the complexity of the scattering processes, the bandstructure and the many optical transitions involved, Monte Carlo theory is one of the only ways to interpret differential transmission measurements. This approach also has the advantage that it lets us separate the data into contributions from different carrier types.

Our results are consistent with $D_{\Gamma-L} = 5 \times 10^8 \, eV/cm$. We have shown, however, that the precise determination of the deformation potential constant is complicated by two effects. First, if the split off transition is energetically allowed, it produces a large contribution to the experimentally measured differential transmission which masks the effects of intervalley scattering. Second, Monte Carlo simulations show that the differential transmission is sensitive to parameters such as the laser bandwidth.

5.4 References

[1]   M. Ulman, D. W. Bailey, L. H. Acioli, F. G. Vallee, C. J. Stanton, E. P. Ippen, and J. G. Fujimoto, "Femtosecond tunable nonlinear absorption spectroscopy in $Al_{0.1}Ga_{0.9}As$," Physical Review B, **47**, p. 10267-10278 (1993).

[2]   J. P. Heritage, A. M. Weiner, and R. N. Thurston, "Picosecond pulse shaping by spectral phase and amplitude manipulation," Optics Letters **10**, p. 609 (1985).

[3]   E. B Treacy, "Optical pulse compression with diffraction gratings," IEEE Journal of Quantum Electronics **5**, p. 454 (1969).

[4]   A. M. Weiner, D. E. Laird, J. S. Patel, and J. R. Wullert, "Programmable femtosecond pulse shaping by use of a multielement liquid crystal phase modulator," Optics Letters **15**, p. 326 (1990).

[5]   D. W. Bailey and C. J. Stanton, "Carrier diffusion effects in time-resolved photoluminescence," Applied Physics Letters, **60**, p. 880-882 (1992).

Chapter 6
Hot carrier dynamics in the presence of a cold background plasma

6.0 Introduction

In this chapter we describe an experiment in which we investigate the dynamics of photoexcited hot carriers in the presence of a cold background carrier population [1]. The motivations for this experiment are both fundamental and practical.

There has been active fundamental interest [2][3][4] in electron dynamics at high densities. Much of this work has been in metals. For a long time it was believed that non-Fermi electron distributions would have to be extremely short lived in metals because the electron density and carrier-carrier scattering rate are high. As shown below our experiment is sensitive to carrier-carrier scattering and provides a way to measure its effectiveness in redistributing carriers.

The practical interest in dynamics between hot carriers and a cold background arises because that is the situation found in experiments on doide lasers. Since diode lasers are extensively used in fiber optic communications and switching, research on their transient response has been intense. Many experiments have been performed which measure ultrafast gain and refractive index changes in diode lasers and active waveguides at 830 nm [5][6][7][8][9][10] and 1.55 um [11][12].

The diode laser experiments are limited in time resolution to about 100 fs because of high dispersion in the diode itself. The critical pulse width is typically 100 fs for a 300 um long diode. By contrast, our

samples are only 0.2 um thick, so dispersion is not a problem. We expect that measurements in thin samples will permit studies with 10 fs time resolution.

6.1 Experiment

We use our CPM laser to generate 50 fs pulses at 2 eV (620 nm). For this set of experiments we "tune" the sample bandstructure instead of the laser wavelength. Thus we studied two different alloys: GaAs and $Al_{0.2}Ga_{0.8}As$. We also illuminate the sample with a CPM pulse a few hundred picoseconds before performing our pump-probe measurement. It is this third pulse or "prepulse" that creates the background population.

Fig. 6.1
Three pulse
pump probe setup
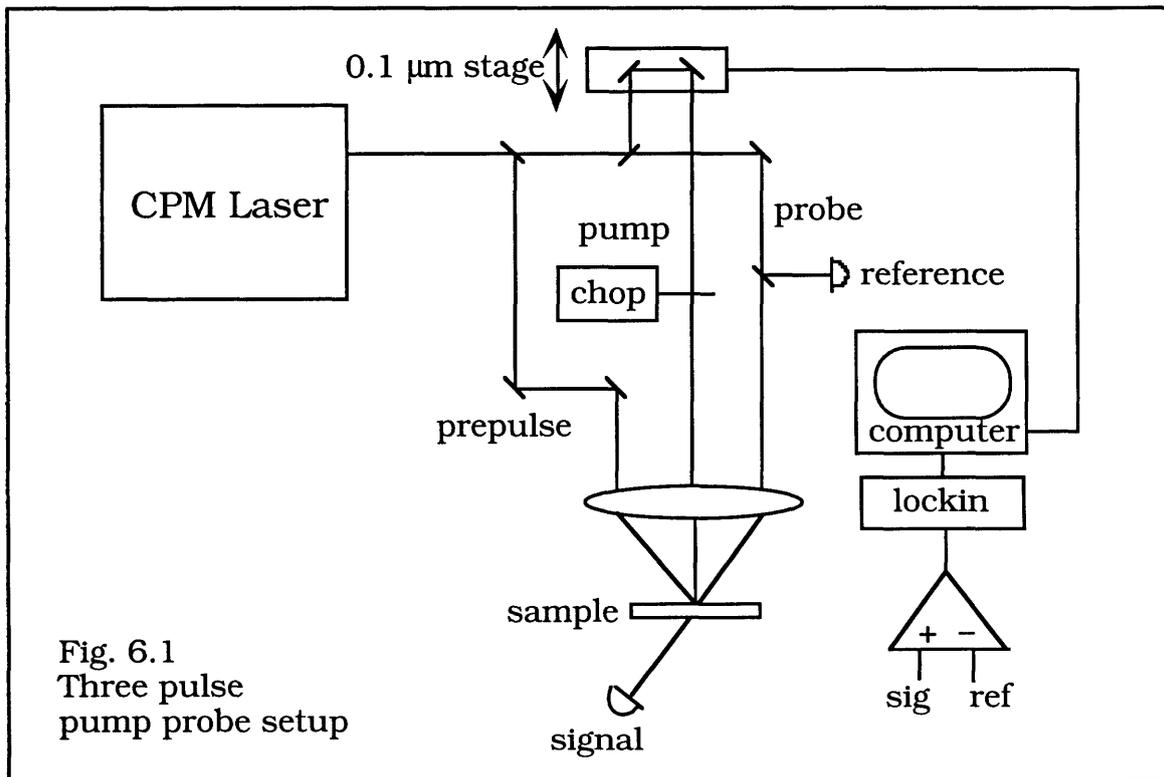
The optical system consist of the CPM laser and a three arm pump-probe delay setup [Figure 6.1]. The pump and probe beams are polarized

perpendicular to each other. They are focussed by a 20X microscope objective to a 6 um diameter spot on the sample. The pump beam is chopped and pump induced changes in the probe are detected with a lockin amplifier in a manner similar to that described in the previous chapter. The prepulse is set to arrive at the sample 350 ps before the pump pulse. This is long enough for the carriers it generates to thermalize and cool to the lattice temperature but shorter than the recombination time. The carrier density of the resulting cold plasma is $1 \times 10^{18} cm^{-3}$ which is about 15 times greater than the hot carrier density which is $7 \times 10^{16} cm^{-3}$.

When the pump pulse is incident on the sample it generates a nonequilibrium carrier distribution via interband absorption. Carriers quickly scatter from their initial states. For sufficiently high excess electron energies, electrons may scatter between the Γ valley and the L and X satellite valleys in the conduction band. In our experiment the pump and probe pulses are at 620 nm or 2 eV. Therefore the initial electron distributions are triply peaked corresponding to transitions from the heavy hole, light hole, and spin split off hole bands [Figure 6.2]. The elecrons from the heavy and light hole transitions are excited high enough in the Γ valley for intervalley scattering to occur. The split off transition lies near the bottom of the band in $Al_{0.2}Ga_{0.8}As$ while in GaAs it creates electrons with approximately 170 meV excess energy. An important difference between the two samples is the position of the split off transition compared to the Fermi level of the cold population created by the prepulse. In GaAs the split off transition is above the Fermi level while in $Al_{0.2}Ga_{0.8}As$ it is below the Fermi level.
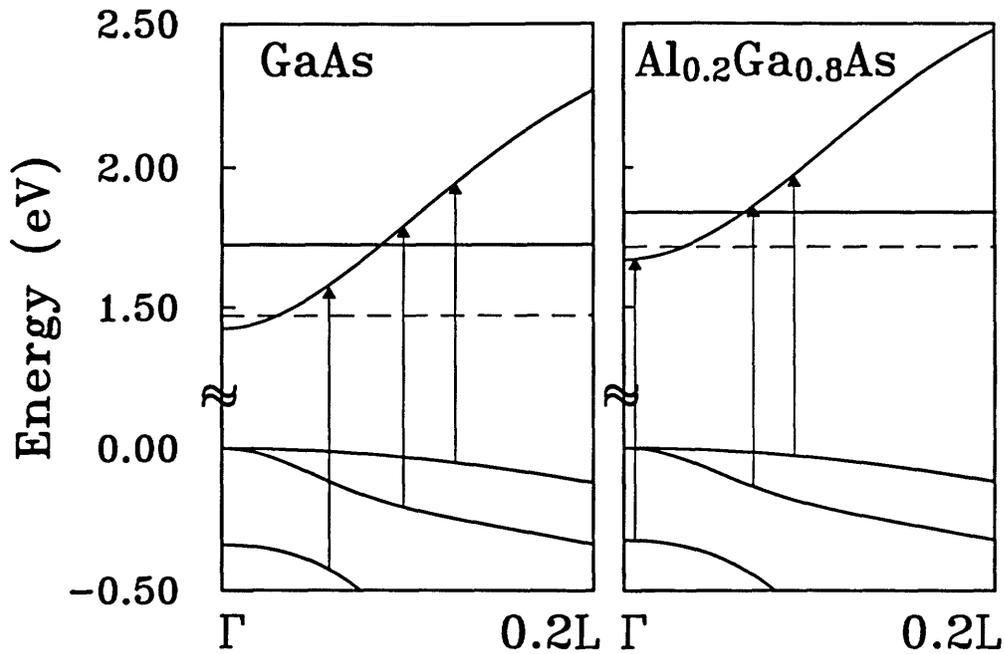
Fig. 6.2 Detail of GaAs and AlGaAs bandstructure showing 2 eV optical transitions. The solid horizontal line indicates the minimum energy in the L satellite valley while the dashed horizontal line shows the quasi Fermi level for a photoexcited electron density of 10^{18} cm^{-3}.

We can see the expected effect on the probe transmission for the two samples [Figure 6.3]. Consider probe delays after the initial hole burning transient: from 200 fs to 1 ps. As electrons redistribute themselves and cool toward the bottom of the band the occupation probed by the split off transition dominates the pump-probe signal. In a traditional empty band experiment the split off transition is sensitive to bandfilling, i.e. carriers accumulating in states at the bottom of the band as they lose energy, carrier cooling, and the return of carriers that scattered out to the satellite valleys. In GaAs the split off transition probes at an energy about 170 meV above the band edge. In this case for pump densities of order 10^{16} to 10^{17} cm^{-3} band filling and carrier cooling produce opposite effects on the pump-probe signal. Band filling increases occupation and therefore in increases transmission. Carrier cooling is a larger effect, however, and decreases the signal since the optical transition is above the Fermi level. Transmission is also

92

enhanced by the return of hot carriers from the L valley. This leads to the observed slow picosecond decay. In $Al_{0.2}Ga_{0.8}As$ both band filling and carrier cooling increase the occupation number of the probed states. Therefore the "slow" behavior starting at 200 fs is a rising transmission as a function of probe delay.

Fig. 6.3 Occupation of electron states in Γ

Cold background
at lattice temp

Hot carriers

F

influence of heating

E

split off transition
in AlGaAs
heating reduces
occupation

split off transition
in GaAs
heating increases
occupation

minimum energy
in L valley
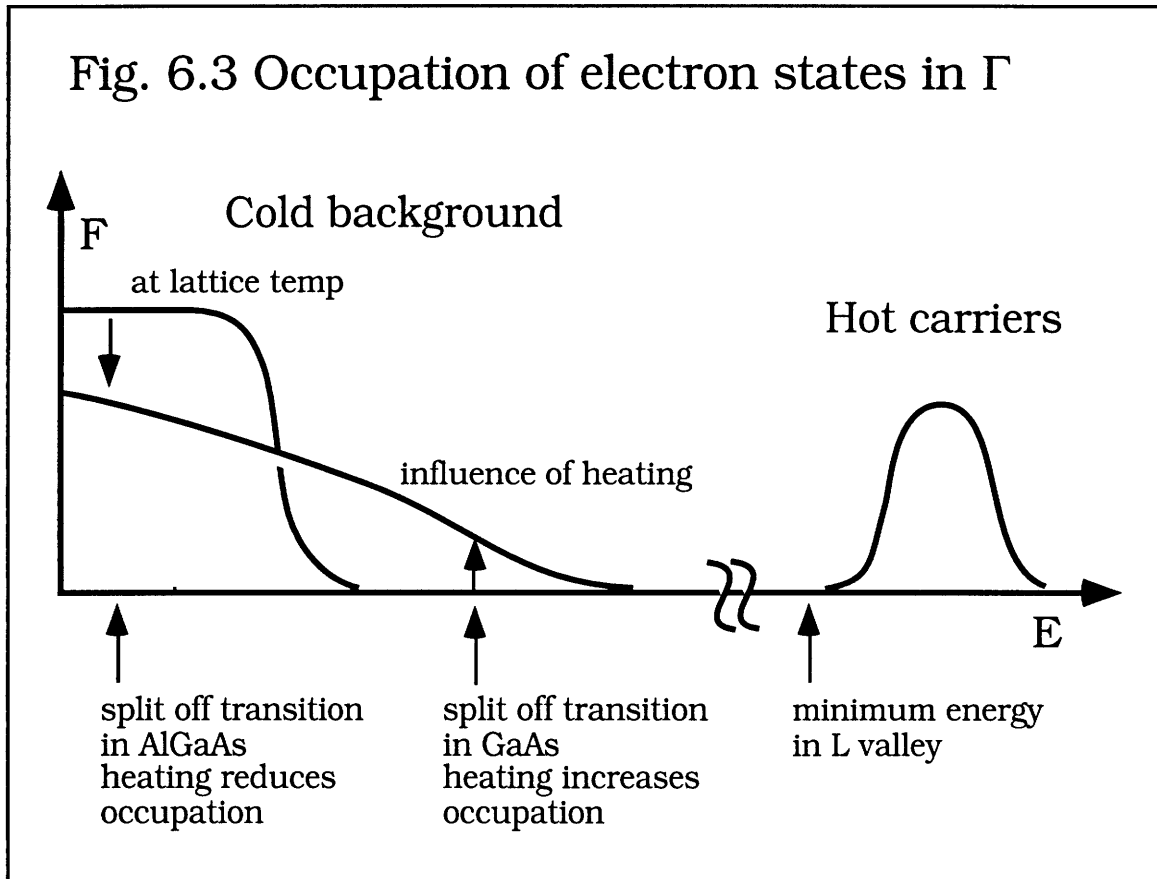
The transient changes in transmission should be different if a cold carrier population already exists at the bottom of the band when the pump-probe experiment is performed. Now the split off transition detects heating and cooling of the cold population as well as bandfilling effects. When we set the prepulse intensity to create a cold carrier density of $1 \times 10^{18} cm^{-3}$ the split off transition probes the occupation of states below the cold carrier Fermi level in $Al_{0.2}Ga_{0.8}As$ and above the Fermi level in GaAs. In $Al_{0.2}Ga_{0.8}As$ any heating of the cold carriers that may occur

will reduce the occupation of states that are probed by the split off transition while band filling increases the occupation. In GaAs both effects increase occupation.

The timing of temperature changes in the cold population should depend on the strengths of the dominant scattering channels: carrier-carrier scattering, polar optic phonon scattering, intervalley scattering, and possibly plasmon scattering. One might guess that carrier-carrier scattering will be especially important since the cold carrier density is high. With these possibilities in mind, we are ready to discuss the actual results.

6.2 Results and discussion

We present our results in Figures 6.4 and 6.5. The traces for normal pump-probe conditions without a prepulse are marked "empty band." These data are commensurate with previously published work [13]. The empty band traces exhibit a fast hole burning transient which decays in about 35 fs in GaAs and 70 fs in $Al_{0.2}Ga_{0.8}As$. The peak decays because electrons scatter out of their initial states mainly by carrier-carrier scattering and intervalley scatering.

After the initial transient in GaAs we see a slow picosecond decay which may be attributed to carrier cooling and the return of carriers from the L valley. In GaAs, electrons are probed 170 meV above the band edge by the split off transition so bandfilling and carrier cooling produce opposite effects. In $Al_{0.2}Ga_{0.8}As$ the split off transition probes near the bottom of the band so bandfilling and carrier cooling both tend to increase differential transmission. We observe a picosecond rise as carriers return from L. As an aside, we note that this rise is an example

94

of a characteristic that cannot be easily modelled by fitting exponential time constants.
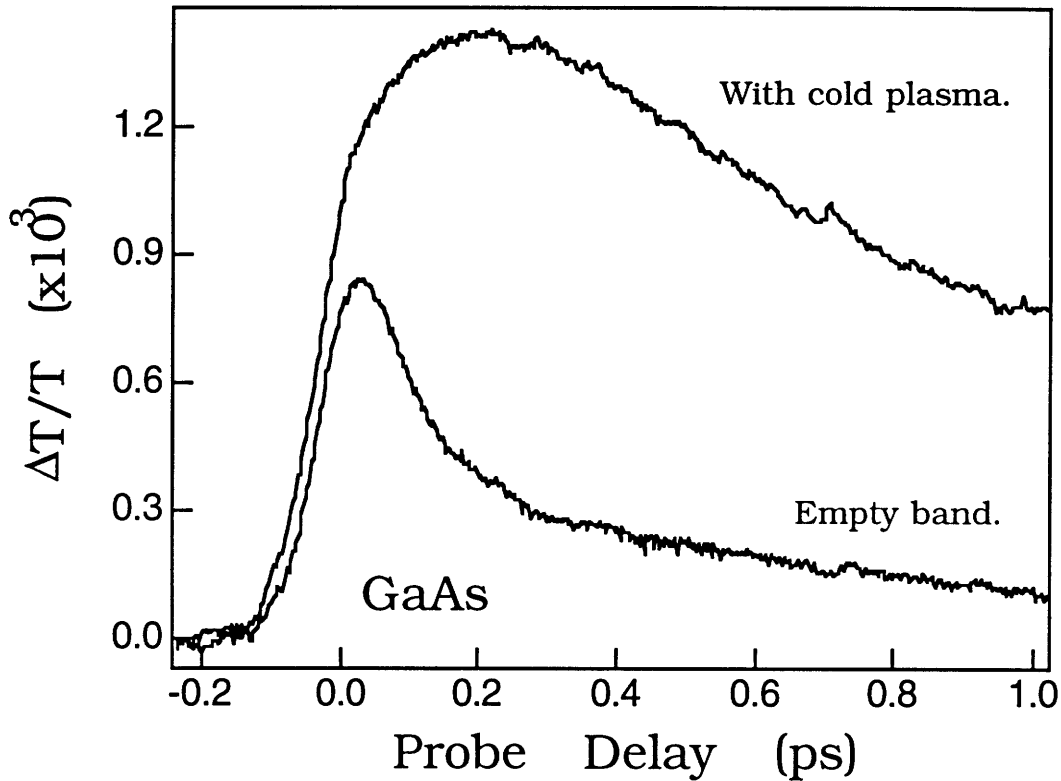

Fig. 6.4 Differential transmission in GaAs under empty band conditions and in the presence of a cold plasma.

When the cold background plasma is present we see different transient absorption behavior. First we consider $Al_{0.2}Ga_{0.8}As$. Here we observe the amplitude of the fast transient decreases by approximately 20 %. This may be phenomenologically attributed to the relaxation time decrease to 40 fs from 70 fs. The overall shape of the transmission data is similar to the empty band data, however. The data indicate that the interaction between the hot and cold electrons has only a small effect on the scattering from initial states. After 200 fs probe delay we see a slow rise just as in the empty band case. In $Al_{0.2}Ga_{0.8}As$ carriers return from the L valley with approximately 150 meV energy which is close to the

average energy of the cold carriers. Therefore the carriers coming back from L only heat the cold population by a small amount. While heating reduces the occupation of states probed by the split off band, band filling increases it. The net effect is that the transmission rises on a picosecond scale.
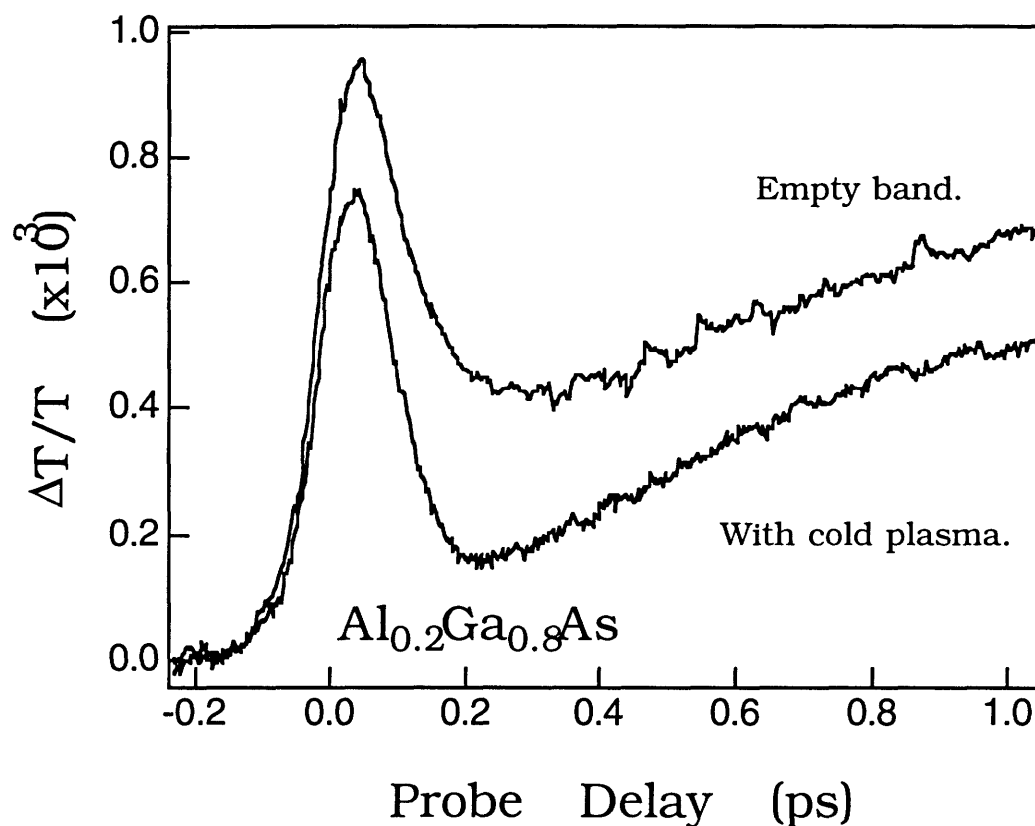

Fig. 6.5 Differential transmission in AlGaAs under empty band conditions and in the presence of a cold plasma.

In GaAs there is a significant difference between the empty band results and those in the presence of the cold background plasma. We observe the transmission rising in approximately 300 fs to a peak value 70 % higher than in the empty band case followed by a picosecond decay. It is important to note that the transmission continues to rise after the pump pulse is over. These data and those for $Al_{0.2}Ga_{0.8}As$ are consistent with a slow heating of the cold carriers. Therefore intervalley

scattering must redistribute the hot carriers faster than hot carrier - cold carrier scattering heats the cold distribution. The 300 fs rise results from a combination of weak hole burning and the slow rise caused by cold carrier heating. In GaAs carriers return from L with about 250 meV energies. This is higher above the Fermi level than in $Al_{0.2}Ga_{0.8}As$ so the heating effect is more pronounced. Furthermore, in GaAs both heating and bandfilling increase transmission.

Our results are different from some other measurements in the recent literature. For example, thermalization times as short as 10 fs have been estimated for modulation doped quantum wells [14]. That experiment is different from ours, however, because there the hot carriers had only small excess energies over the cold carriers.

We have tried to model this experiment using the Monte Carlo method described in Chapter 4 and applied in Chapter 5. To date we have met with only limited success. The main problem is that the Monte Carlo simulation spends most of its time scattering the cold carriers which are near equilibrium [15]. Only a few of the simulation electrons represent the hot carriers. This leads to high noise levels. In our attempts so far, the noise has been too great to permit interpretation of the simulation results.

One way around this problem is to model the cold carriers with a thermal distribution function and use the particle simulation for the hot carriers only. In this approach, however, it is impossible to account for hot carrier - cold carrier scattering which we believe is an important effect in the experiment.

6.3 Conclusions

97

We performed an investigation of femtosecond carrier dynamics in GaAs and AlGaAs in the presence of a cold carrier background population. In this experiment, one of the main features was that we varied the sample bandstructure instead of tuning the laser wavelength. This was accomplished by taking advantage of the property of $Al_xGa_{1-x}As$ that the band gap increases linearly with x. We were therefore able to perform experiments using only the CPM laser which provides much better signal to noise performance than the amplified system used in the experiments described in chapter 5. The other essential point in this work was that we illuminated the sample with a third laser pulse a few hundred picoseconds before performing the pump-probe experiment. This third pulse excited a population that became a cold background carrier distribution by the time the pump-probe experiment was performed. We used this situation to study the effect of a cold distribution on the thermalization of hot carriers. One of the practical motivations for this experment is that it is analogous to diode laser experiments in which the cold background carriers are brought into the system by a wire. The advantage of our technique is that we study thin samples where dispersion is not a problem.

Our results led to the conclusion that, in the system we studied, the effect of the cold carriers on the hot carrier thermalization rate is slower than intervalley scattering. At first this seems like a suprising result because carrier-carrier scattering is a fast process. Carrier scattering is always limited by the availability of final states to scatter into, however. Pauli exclusion severely constrains the effectiveness of carrier-carrier scattering when a large number of states are filled near the bottom of the band, as is the case in this experiment.

Finally, we did not present Monte Carlo simulations of the carrier dynamics for this experiment. Some simulations have already been performed. They are so noisy that they are unusable at this point, however. The high noise exists because the simulation spends most of its time tracking the large number of cold carriers. It may be possible to overcome this problem by representing the cold carriers with a Fermi distribution function, and work in this direction is ongoing.

6.4 References

[1]   L. H. Acioli, M. Ulman, F. Vallee, and J. G. Fujimoto, "Femtosecond carrier dynamics in the presence of a cold plasma in GaAs and AlGaAs," Applied Physics Letters **63**, p. 666 (1993).

[2]   R. W. Schoenlein, W. Lin, J. G. Fujimoto, and G. Eesley, Physical Review Letters **58**, p. 1680 (1987).

[3]   C. K. Sun, F. Vallee, L. Acioli, E. P. Ippen, and J. G. Fujimoto, "Femtosecond investigation of electron thermalization in gold," Physical Review B **48**, p. 12365 (1993).

[4]   W. S. Fann *et al.*, Physical Review Letters **68**, p. 2834 (1992)

[5]   M. P. Kesler and E. P. Ippen, "Subpicosecond gain dynamics in GaAlAs laser diodes," Applied Physics Letters **51**, p. 1765 (1987).

[6]   K. K. Anderson, M. J. LaGasse, C. A. Wang, J. G. Fujimoto, and H. A. Haus, "Femtosecond dynamics of the nonlinear index near the band edge in AlGaAs waveguides," Applied Physics Letters **56**, p. 1834 (1990).

[7]   M. J. LaGasse, K. K. Anderson, C. A. Wang, J. G. Fujimoto, and H. A. Haus, "Femtosecond measurements of the nonresonant nonliear index in AlGaAs," Applied Physics Letters **56**, p. 417 (1990).

[8] C. T. Hultgren and E. P. Ippen, "Ultrafast refractive index dynamics in AlGaAs diode laser amplifiers," Applied Physics Letters **59**, p. 635 (1991).

[9] C. T. Hultgren, D. J. Dougherty, and E. P. Ippen, "Above- and below-band femtosecond nonlinearities in active AlGaAs waveguides," Applied Physics Letters **61**, p. 2767 (1992).

[10] C. K. Sun, H. K. Choi, C. A. Wang, and J. G. Fujimoto, "Studies of carrier heating in InGaAs/AlGaAs strained-layer quantum well diode lasers using a multiple wavelength pump probe technique," Applied Physics Letters **62**, p. 747 (1993).

[11] K. L. Hall, Y. Lai, E. P. Ippen, G. Eisenstein, and U. Koren, "Femtosecond gain dynamics and saturation behavior in InGaAsP multiple quantum well optical amplifiers," Applied Physics Letters **57**, p. 2888 (1990).

[12] K. L. Hall, A. M. Darwish, E. P. Ippen, U. Koren, and G. Raybon, "Femtosecond index nonlinearities in InGaAsP optical amplifiers," Applied Physics Letters **62**, p. 1320 (1993).

[13] W. Z. Lin, R. W. Schoenlein, J. G. Fujimoto, and E. P. Ippen, "Femtosecond absorption saturation studies of hot carriers in GaAs and AlGaAs," IEEE Journal of Quantum Electronics **24**, p. 267 (1988).

[14] W. H. Knox, D. S. Chemla, G. Livescu, J. E. Cunningham, and J. E. Henry, Physical Review Letters **61**, p. 1290 (1988).

[15] C. J. Stanton, private communication.

Chapter 7
Conclusion

7.0 Conclusion

We have presented a series of femtosecond laser based experiments on GaAs and AlGaAs. The main goal of the work was to increase our knowledge of femtosecond carrier dynamics in these semiconductors. Our approach has been to combine state of the art femtosecond spectroscopy with theoretical ensemble Monte Carlo simulations.

We used a colliding pulse modelocked ring dye laser amplified by a copper vapor laser pumped dye amplifier as a source of femtosecond optical pulses. These pulses were modified by linear and nonlinear optical techniques and incorporated in a pump-probe nonlinear differential transmission measurement scheme. The data that we collected are measurements of pump pulse induced changes in the transmission of a probe pulse through a thin sample. The samples are bulk GaAs and AlGaAs grown by molecular beam epitaxy at MIT Lincoln Laboratory. Our experimental system has 40 fs time resolution which allows us to examine carrier dynamics on the same time scale that fundamental scattering processes occur.

We collaborated with theoretical solid state physicists at the University of Florida for help in interpreting our data. Ensemble Monte Carlo simulations were used to model the ultrafast carrier dynamics in the semiconductor. Our Monte Carlo simulation incorporates a realistic full bandstructure calculation and an algorithm to predict the experimentally observed differential transmission behavior. The Monte

Carlo method is the only way to extract the temporal behavior of the nonequilibrium carrier distribution functions from pump-probe data. It is also a powerful technique because it allows us to artificially separate the effects of various scattering processes.

We addressed the dynamics of scattering from initial states from 1.7 eV to 1.9 eV in $Al_{0.1}Ga_{0.9}As$ and of hot carrier - cold carrier interactions in GaAs and $Al_{0.2}Ga_{0.8}As$. In $Al_{0.1}Ga_{0.9}As$ we investigated a region of the bandstructure that had not been covered in band edge studies or 2 eV laser based experiments. We designed the experiment to be sensitive to intervalley scattering and fit our data with the deformation potential constant, $D_{\Gamma-L} = 5 \times 10^8 eV / cm$. The theoretical model fits the data well over the full 200 meV investigated. It is plausible, therefore, that the model will be suitable to predict device behavior in the future. We used a new three pulse technique to investigate the dynamics of hot carriers in the presence of a cold background plasma in GaAs and $Al_{0.2}Ga_{0.8}As$. Here we made the interesting conclusion that heating of cold carriers by hot carriers takes place more slowly than intervalley scattering for the conditions in our experiment. We also discovered that our Monte Carlo method will need to be extended to model this experiment. Because the cold carrier density is much greater than that of the hot carriers, the simulation spends most of its time tracking cold carriers. The result is that the simulation of hot carriers is too noisy to be useful. Theoretical work on this problem continues.

This work has helped to establish a foundation for future experimental and theoretical studies of femtosecond carrier dynamics in semiconductors.

7.1 Suggestions for future work

The study of femtosecond dynamics in GaAs and other semiconductors is by now a well trodden path. The future most likely lies in artificial quantum confined structures and optoelectronic devices. Only a few experiments remain in bulk samples.

The recent success of the Ti:Sapphire laser for femtosecond pulse generation suggests that experiments similar to those described in chapter 6 could be performed at longer wavelengths. A useful experiment would be to perform a three pulse study in $Al_{0.1}Ga_{0.9}As$ using a cavity dumped Ti:Sapphire laser. The bandgap of $Al_{0.1}Ga_{0.9}As$ is at 800 nm which is near the center wavelength of the Ti:Sapphire laser. The cavity dumped system has the advantages of appropriate repetition rate, high stability, and enough power to generate a broadband or continuum probe pulse. Improved time resolution is another realizable benefit. Recent three pulse experiments have been performed by Peyghambarian's group [1]

ZnSe and GaN are important semiconductors for blue diode lasers. A frequency doubled Ti:sapphire laser could be used to invesigate carrier dynamics in these wide bandgap materials. Experiments on ZnSe have already begun at MIT.

7.3 References

[1] K. Meissner, B. Fluegel, H. Geissen, B. P. McGinnis, A. Paul, R. Binder, S. W. Koch, N. Peyghambarian, M. Grun, and C. Klingshirn, "Spectral hole burning in the gain region of an inverted semiconductor," Physical Review B **48**, p. 15472 (1993).

Appendix A
Applications of femtosecond pulses in scanning tunneling microscopy

A.0 Introduction

The scanning tunneling microscope was invented in 1981 by Binnig and Rohrer at IBM's Zurich research lab. It provides the highest spatial resolution of any microscope; one can see individual atoms. It quickly became a powerful research tool and won its inventors the 1986 Nobel prize in physics. Nowadays one can purchase STM systems from dozens of manufacturers. The femtosecond pulsed laser was invented by Ippen and Shank at AT&T Bell Laboratories in 1972. Recently the femtosecond Ti:Sapphire laser has provided wavelength tunable 10 fs performance from an easy to use system. Femtosecond laser pulses are the basis for the highest direct time resolution experiments.

Any research strategy that is based on creating new measurement capability is guaranteed to produce results. Since it appears that maintaining laser superiority over our scientific competitors is becoming harder and harder, we are simultaneously committed to another strategy: combining established measurement technologies in new ways. This has already worked well in the case of photoemission and femtosecond lasers which were combined by Schoenlein to measure image potential state dynamics in metals [1]. We have recently begun work to combine femtosecond lasers with scanning tunneling microscopy in an attempt to make measurements that are highly localized in space and time. Here we present preliminary results from that effort.

A.1 Work in other labs

Several other groups have also begun work in the direction of femtosecond STM. The first of these was Walther's group who studied the frequency mixing properties of the tunneling juntion in 1987 [2]. They detected difference frequencies up to 90 MHz from two CO_2 lasers measured the dependence of the beat signal on the bias voltage. They attributed the beat signal to thermally assisted tunneling at low bias voltages and to the behavior of the gap as a point contact diode at high bias. Later [3] they used the beat signal to drive the feedback circuit of an STM so that no external bias was necessary. They suggested that their technique could be used to study insulators, although AFM is of course ideally suited for that purpose.

Another interesting application of lasers to STM is photothermal modulation of the tip sample distance which was first reported by Amer et al. [4]. The effect was studied up to modulation frequencies of 100 kHz.

Bloom's group used an AFM to sample picosecond electrical signals [5]. They took advantage of the fact that the force between the AFM tip and the sample surface (modelled as a parallel plate capacitor) depends on the square of the voltage between them. They were able to observe frequency mixing of sinusoidal electrical signals at frequencies up to 20 GHz and sample 130 ps pulses travelling on a coplanar waveguide transmission line. Recently they have applied their technique to detecting signals on high speed microprocessor integrated circuits [6].

Several groups have tried to gate the signals from an STM [7][8][9][10]. Weiss et al. used Si on sapphire switches to gate the

tunneling current and performed a cross correlation with an electrical pulse launched on a microwave transmission line. Takeuchi et al. used a similar apparatus in which the photoconductive switch was mounted very close to the tunneling tip. They used their device to measure 300 ps electrical waveforms on a gold microstrip line. Nunes and Freeman used an STM to correlate two electrical pulses launched on the same transmission line. The time resolved tunneling current is a result of nonlinearity in the STM current versus voltage characteristic, $J \sim \beta(V + \gamma V^3)$. β and γ are constants which depend on the average barrier height and the tip-sample separation. A cross correlation of picosecond voltage pulses yielded a signal with a FWHM of 130 ps.

A.2 Experiments

We have constructed a system for exploring femtosecond STM. Our microscope consists of a commercial piezoelectric tube scanner (Digital Instruments), a home built coarse approach mechanism, and a home built feedback loop. We use a colliding pulse modelocked ring dye laser amplified by a frequency doubled, Q-switched Nd:YLF laser pumped dye amplifier as a source of intense femtosecond optical pulses. After sending the optical pulses through an equal pulse correlation delay setup we focus them on the STM tip with a 10 X microscope objective. With this system we are able to record, for example, the tunneling current versus delay between two femtosecond optical pulses illuminating the tip.

A.3 Results and discussion

We have observed what appears to be the interferometric autocorrelation of our laser pulses by recording the optically induced

part of the tunneling current versus delay between two identical pulses. Another group recently reported similar results [11].

Fig. A.1 Tunnel current versus delay between two optical pulses.
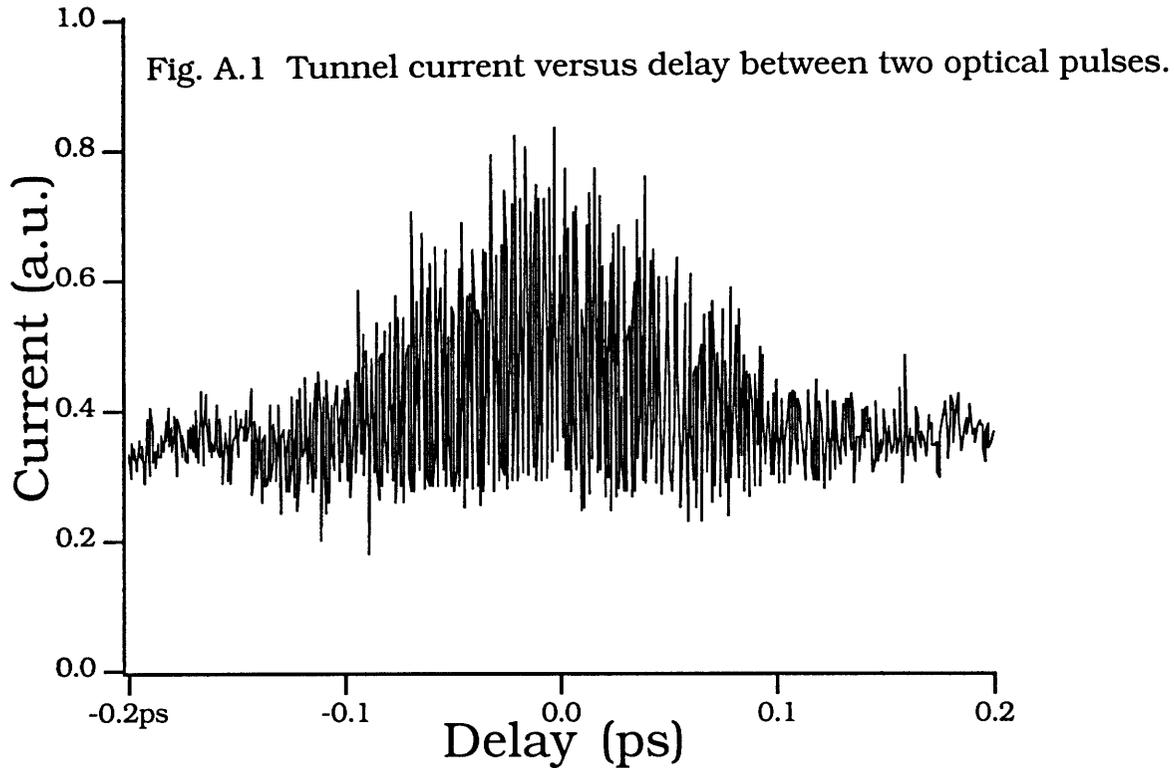
We have observed signals in two different bias regimes. In the first scenario we use biases that are higher than the work function of the tip. This leads to photoemission of electrons which are collected at the sample. In the other scenario we use normal, millivolt biases. Here, the optical pulse heats the electron distribution in the tip and induces thermally assisted tunneling. Work is now proceeding to try to detect short voltage pulses on a microwave stripline in the photoemission bias regime.

A.4 Conclusion

Femtosecond STM promises to be an exciting area of research. No one has yet demonstrated atomic size and femtosecond time resolution

simultaneously. Once that capability is demonstrated and developed, many applications in science and engineering will follow.

A.5 References

[1]   R. W. Schoenlein, J. G. Fujimoto, G. L. Eesley, and T. W. Capehart, "Femtosecond relaxation dynamics of image potential states," Physical Review B **43**, p. 4688 (1991).

[2]   L. Arnold, W. Krieger, and H. Walther, "Laser frequency mixing in the junction of a scanning tunneling microscope," Applied Physics Letters **51**, p. 786 (1987).

[3]   M. Volcker, W. Krieger, and H. Walther, "Laser driven scanning tunneling microscope," Physical Review Letters **66**, p. 1717 (1991).

[4]   N. M. Amer, A. Skumanich, and D. Ripple, "Photothermal modulation of the gap distance in scanning tunneling microscopy," Applied Physics Letters **49**, p. 137 (1986).

[5]   A. S. Hou, F. Ho, and D. M. Bloom, "Picosecond electrical sampling using a scanning force microscope," Electronics Letters **28**, p. 2302 (1992).

[6]   D. M. Bloom, A. S. Hou, and F. Ho, Ultrafast Phenomena Conference, Dana Point, CA, May 2-6, 1994.

[7]   S. Weiss, D. F. Ogeltree, D. Botkin, M. Salmeron, and D. S. Chemla, "Ultrafast scanning probe microscopy," Applied Physics Letters **63**, p. 2567 (1993).

[8]   M. R. Freeman and G. Nunes, "Time resolved scanning tunneling microscopy through tunnel distance modulation," Applied Physics Letters **63**, p. 2633 (1993).

[9]   K. Takeuchi and Y. Kasahara, "High speed optical sampling measurement of electrical wave form using a scanning tunneling microscope," Applied Physics Letters **63**, p. 3548 (1993).

[10]   G. Nunes and M. R. Freeman, "Picosecond resolution in scanning tunneling microscopy," Science **262**, p. 1029 (1993).

[11]   G. Gerber, F. Sattler, S. Vogler, J. Y. Grand, P. Leiderer, and R. Moller, "Femtosecond time resolution in scanning tunneling microscopy," Ultrafast Phenomena Conference, Dana Point, CA, May 2-6, 1994.